SANDIA REPORT

SAND99-2758
Unlimited Release
Printed November 1999

Modeling Decomposition of Unconfined Rigid Polyurethane Foam

Michael L. Hobbs, Kenneth L. Erickson, and Tze Y. Chu

Prepared by
Sandia National Laboratories
Albuquerque, New Mexico 87185 and Livermore, California 94550

Sandia is a multiprogram laboratory operated by Sandia Corporation, a Lockheed Martin Company, for the United States Department of Energy under Contract DE-AC04-94AL85000.

Sandia National Laboratories

Inside front cover (disclaimer goes here)

SAND99-2758
Unlimited Release
Printed November 1999

Modeling Decomposition of Unconfined Rigid Polyurethane Foam

Michael L. Hobbs, Kenneth L. Erickson, and Tze Y. Chu
Engineering Sciences Center
P. O. Box 5800, Sandia National Laboratories,
Albuquerque, New Mexico 87185-0836

Abstract

The decomposition of unconfined rigid polyurethane foam has been modeled by a kinetic bond-breaking scheme describing degradation of a primary polymer and formation of a thermally stable secondary polymer. The bond-breaking scheme is resolved using percolation theory to describe evolving polymer fragments. The polymer fragments vaporize according to individual vapor pressures. Kinetic parameters for the model were obtained from Thermal Gravimetric Analysis (TGA). The chemical structure of the foam was determined from the preparation techniques and ingredients used to synthesize the foam. Scale-up effects were investigated by simulating the response of an incident heat flux of 25 W/cm^2 on a partially confined 8.8-cm diameter by 15-cm long right circular cylinder of foam which contained an encapsulated component. Predictions of center, midradial, and component temperatures, as well as regression of the foam surface, were in agreement with measurements using thermocouples and X-ray imaging.

Table of Contents

List of Figures

List of Tables

EXECUTIVE SUMMARY

This report describes the decomposition of unconfined rigid polyurethane foam using a kinetic bond-breaking scheme, lattice statistics, and vapor liquid equilibrium. Bond-breaking is based on degradation of a primary polymer and formation of a thermally stable secondary polymer. The bond-breaking scheme is resolved using percolation theory. The polymer fragments vaporize according to individual vapor pressures. This report describes the chemical structure of the polyurethane foam used in this study, the chemical mechanism used to describe bond breaking, the details of the lattice statistics using percolation theory, and the vapor-liquid equilibrium model used to determine the split between liquids and gas formation. The report also describes the method used to determine the kinetic coefficients, a comparison between predicted and measured mass loss for various TGA experiments, an uncertainty and sensitivity analysis of the PUF model, and a comparison between the predicted shape of a regression front and measured shape of the regression front using X-ray tomography. The report ends with a Summary and Conclusions section.

1. INTRODUCTION

Rigid polyurethane foams are used as encapsulants to isolate and support thermally sensitive components within weapon systems. When exposed to abnormal thermal environments, such as fire, various encapsulated components are designed to fail sequentially. In hazards analysis, the thermal response of the encapsulated components depends primarily on the behavior of the foam. Modeling foam decomposition is a difficult problem not only because of the numerical challenges associated with steep reaction fronts but also the difficulty of describing important chemical and physical processes, such as non-Newtonian liquid flow. In the current report, thermal transport

and decomposition chemistry are discussed in detail. Mass transport, species diffusion, bubble mechanics, fluid flow, and gravitational effects are beyond the scope of this report.

In the past, simplifying assumptions regarding the encapsulating foam have been made for predicting component failure. For example, the decomposition of foam has been ignored, by assuming the foam was not present and adjusting surface emissivities to match thermocouple data, or by changing physical properties of the foam at prescribed temperatures. Such approximations were consistent with equivalent approximations necessary for single processor calculations. With the advent of massively parallel computers, high-consequence predictions of foam decomposition can be made with a more fundamental foam decomposition model founded on experimental observations to determine accurate decomposition rates, decomposition species, and physical properties of the evolving solid residue.

Computational models used in hazards analysis at Sandia National Laboratories are designed to accommodate mass loss associated with foam decomposition. For example, Fig. 1 shows a COYOTE[1] finite element calculation of a block of material containing nonreactive components of various shapes exposed to a constant energy flux. In this calculation, the encapsulating material was assumed to decompose by removing elements from the computational domain based on the element exceeding a specified temperature, without using a realistic decomposition mechanism. Actual tests of polyurethane foam exposed to abnormal thermal environments, such as fire, show the system response to be more complex.

Several groups studying the decomposition of large macromolecules have employed statistical network fragmentation models to describe decomposition chemistry. For example, Solomon and coworkers[2] have implemented a computationally intensive Monte Carlo technique to describe the breakup of coal. Grant et al.[3-5] have used pseudo lattice structures, referred to as

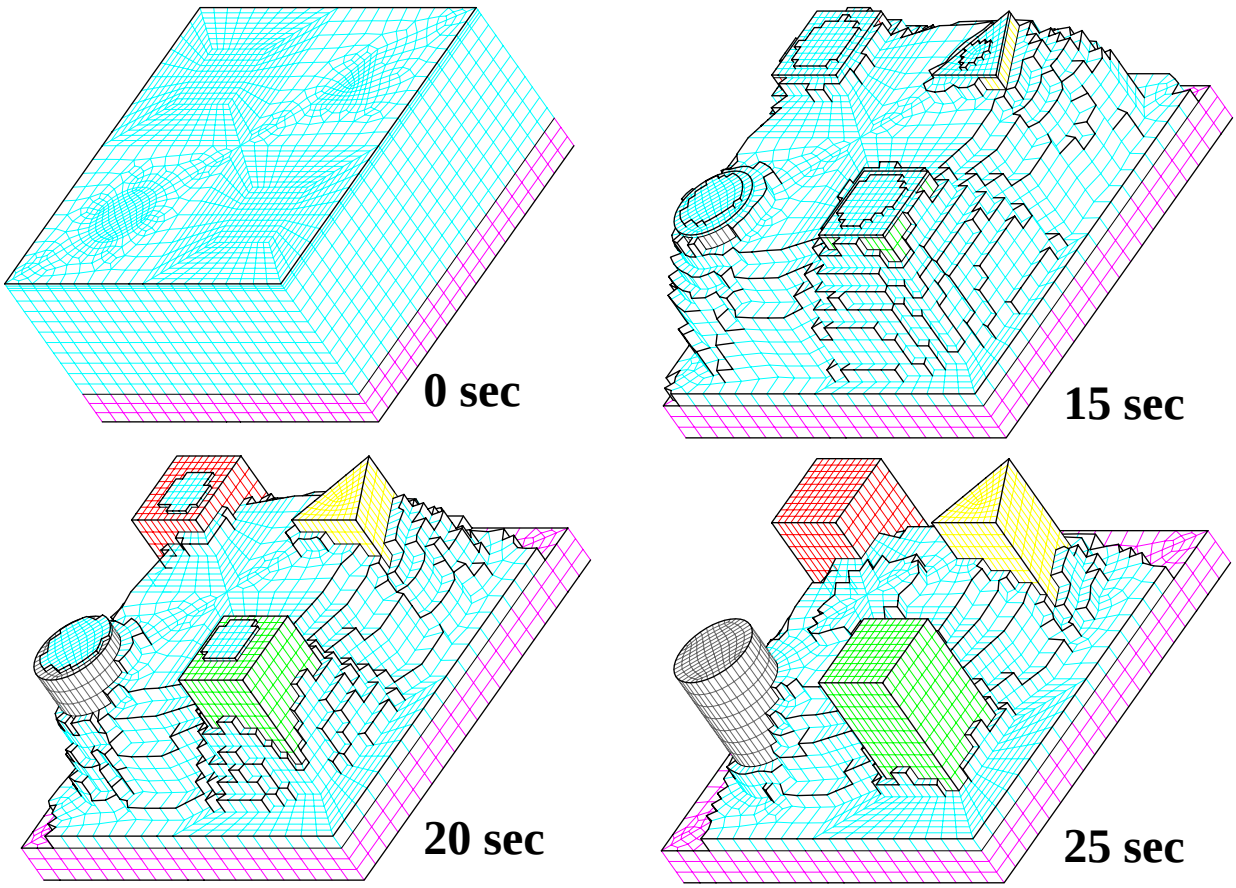

Fig. 1 Example calculation of inert components encapsulated in rigid polyurethane foam initially at 100˚ C exposed to a constant flux on the entire exposed surface. Elements were removed when element temperature exceeded 150˚ C. Although foam regression is shown as a function of time, a decomposition model was not used for this calculation. Figure used with permission from Gartling.[1]

Bethe lattices, to obtain closed-form solutions of the network statistics as derived by Fisher and Essam.[6] These closed form solutions parallel the determination of molecular weight distributions during polymer synthesis leading to the critical condition required to form infinite polymer networks referred to as “gels” by Flory.[7] In the present report, Flory’s methods of building polymers are used to decompose polymers by assuming that closed rings or cycles cannot form and that bond reactivity is independent of the size of the polymer fragment containing the bond. Bond breaking is assumed to be a random scission process that describes the extent of reaction.

The PolyUrethane Foam (PUF) decomposition model discussed in the present report is based on three fundamental aspects of thermal decomposition: 1) a kinetic bond-breaking mechanism, 2) lattice statistics to describe the evolving polymer fragments, and 3) vaporization of the small polymer fragments (oligomers) with high vapor pressures as discussed by Fletcher et al.[4-5] The Bethe lattice statistical model is referred to as *percolation theory,* since the technique has been used historically to describe fluid flow through a network of permeable and impermeable sites. To use percolation theory in a bond-breaking mechanism, the intact bonds correspond to impermeable sites, and the broken bonds correspond to permeable sites. The PUF model parameters include the Arrhenius kinetics - controlling bond-breaking, the initial bridge population, the coordination number, and the average site molecular weight. The initial bridge population is assumed to be composed of both strong bridges and weak bridges (discussed further in Section 3). The coordination number describes the connectivity of thermally stable sites by bridges.

In the current report, the term “polymer” will be used to describe the infinite lattice structure, the term “polymer fragments” refers to the finite fragments resulting from polymer decomposition, and the term “oligomer” will be used to describe the finite fragments that evolve into the gas phase. The term “bridge” is used to represent the part of the polymer structure separating thermally stable “sites.” “Bridges” are connected to “sites” by chemical bonds. When a bond is broken, a bridge is also broken. A more detailed discussion of “bridges,” “sites,” and “bonds” can be found in Section 2.

The remainder of this report is organized as follows: The next section describes the chemical structure of the polyurethane foam used in this study. Section 3 describes the chemical mechanism used to describe bond breaking. Section 4 presents the details of the lattice statistics using percolation theory as applied to bond breaking. Section 5 describes the vapor-liquid equilibrium

model used to determine the split between liquid formation and gas formation. Section 6 discusses the method used to determine the kinetic coefficients for the bond-breaking reactions as well as presents a comparison between predicted and measured mass loss for various TGA experiments. Section 7 presents an uncertainty and sensitivity analysis of the PUF model. Section 8 shows a comparison between the predicted shape of a regression front and shape of the regression front using X-ray tomography. Some general remarks close the report.

2. CHEMICAL STRUCTURE

Detailed information regarding the chemical structure of the polyurethane foam is required to predict foam decomposition using lattice statistics. The structural units and resulting polymeric network of many *synthesized* macromolecules, such as polyurethane foam, can be inferred from the starting materials and the synthesis of the macromolecule. Confirmation of the structure is often obtained using IR spectroscopy, solid-state NMR,[8] and other analytical chemistry techniques.

The most common chemical structural units of the rigid polyurethane foam and the distribution of these structural units are shown in Fig. 2 and were estimated using proprietary synthesis details and assuming equal reactivity of the hydroxyl groups. Various graphic representations of specific chemical structural units are also shown in Fig. 2. These structural units have been assembled to give a representative picture of the foam. The model foam shows the polyurethane structure as a large matrix (essentially infinite) of toluene diisocyanate groups connected by aliphatic bridges made from trimethylol propane, adipic acid, diethylene glycol, and small amounts of phthalic anhydride.

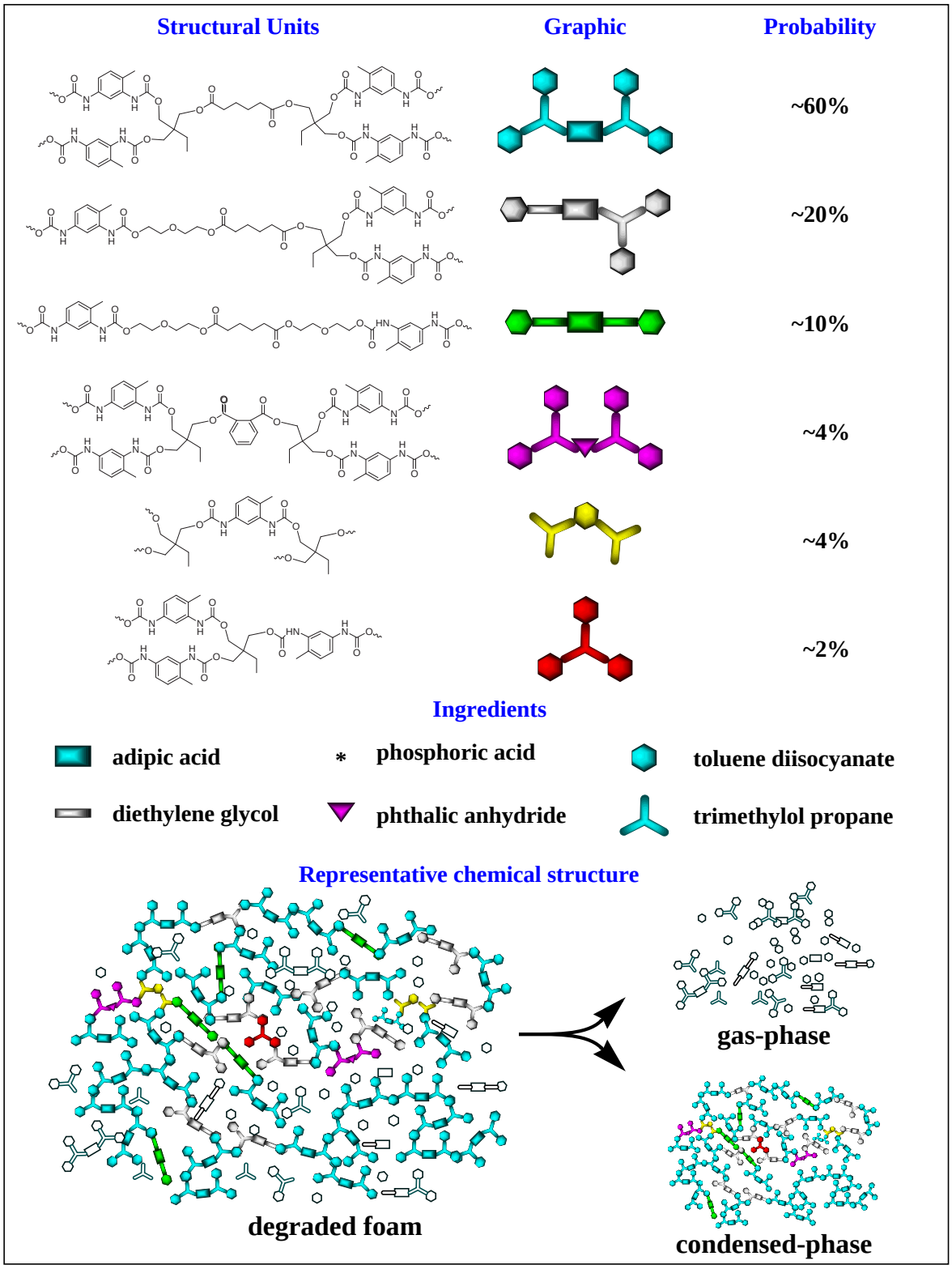

Fig. 2 Most common chemical structural units and hypothetical chemical structure of rigid polyurethane foam. The graphic symbols are composed of ingredients used to make the specific foam.

Figure 3 shows the three most common structural units divided into sites and bridges. The coordination number, $\sigma+1$, and molecular weights for specific structural components are shown in Fig. 3. This information can be used to determine the average coordination number, as well as the average molecular weight of the sites and bridges as discussed further in Section 6. In the present report, the sites are assumed to be primarily composed of trimethylol propane units and the diethylene glycol units. The bridges are composed of the TDI and adipic acid structures.

As the bonds break at elevated temperatures, fragments of finite molecular weight are generated. The fragments, with low molecular weights and corresponding high vapor pressures, evaporate to form gaseous oligomers as shown at the bottom of Fig. 2. Higher molecular weight fragments, with low vapor pressures, remain in the condensed phase.

3. KINETIC MECHANISM

In this study, the initial polymer structure begins to degrade between 250 and 350˚ C as bridges between sites are either broken or become thermally stable via the evolution of light gases, similar to the cellulose decomposition model discussed by Grant et al.[3] and Shafizadeh.[9] At these temperatures, secondary reactions between functional groups can also form bridges between sites, creating a secondary polymer structure. The secondary polymer is assumed to decompose analogously to the primary polymer, but at temperatures above 350˚ C and at a different rate.

The PUF bond decomposition model is an extension of Grant et al.[3] bond-breaking scheme and is the first attempt to describe degradation of a polyurethane foam using percolation theory with vapor liquid equilibrium. All of the PUF model parameters were obtained from data taken near ambient pressures, and the model is not expected to perform well under heavy confine-

A) 60% most probable structural unit of a rigid polyurethane foam

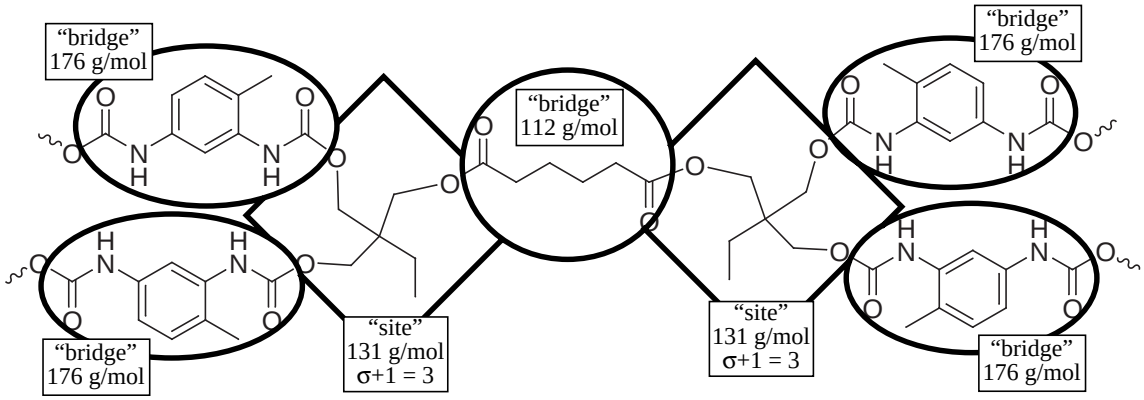

B) 20% most probable structural unit of a rigid polyurethane foam

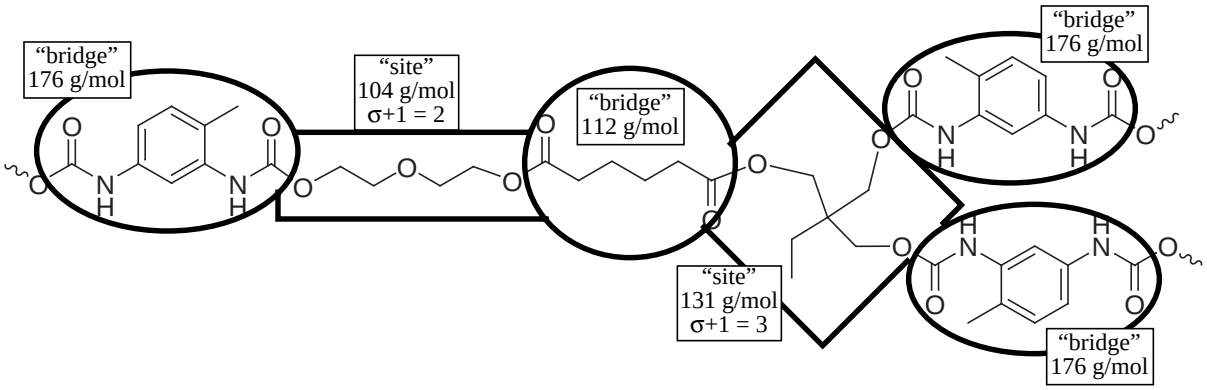

C) 10% most probable structural unit of a rigid polyurethane foam

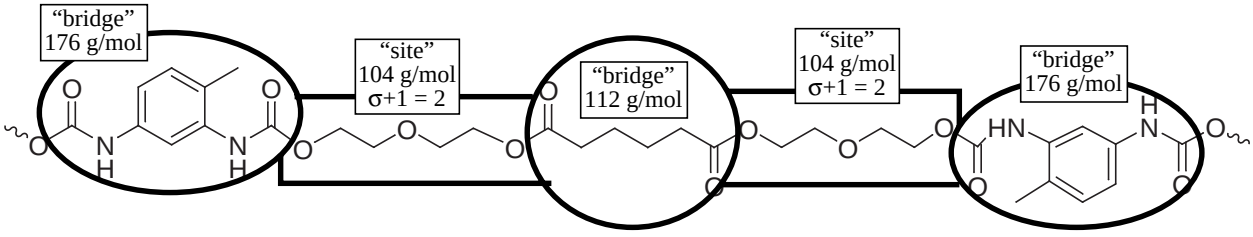

Fig. 3 Three most common structural units of a rigid polyurethane foam showing boundaries used to relate chemical structure to a Bethe lattice.

ment where secondary reactions between the vapor and solid are significant. Currently, an experimental program[10] is being conducted to obtain additional information regarding the decomposition mechanism with attention focused on confinement issues and pressure effects.

The kinetic scheme, along with a graphical description, is shown in Figs. 4 and 5. This 9-step mechanism with 11 "species" describes four events: 1) competition between local crosslinking and side-chain formation within the primary polymer, 2) competition between side-chain evolution from the primary polymer and the formation of a secondary polymer, 3) competition between local crosslinking in the secondary polymer and side-chain formation within the secondary polymer, and 4) side-chain evolution from the secondary polymer.

The L, L, c_1, and c_2 represent bridges as shown in Figs. 4 and 5. A representative labile bridge in the primary polymer, L, is the TDI structural component as shown boxed in Fig. 4. The L bridge is shown in Fig. 4 connecting two trimethylol propane sites with urethane linkages. The labile bridge in the secondary polymer, L, is also shown boxed in Figs. 4 and 5. The L bridge is composed of two toluene components linked by a carbodiimide group, ~N=C=N~. The L bridge is connected to the polymer by two urethane linkages. Thermally stable bridges that connect sites, c_1 and c_2, are shown in Figs. 4 and 5. The thermally stable bridges are actually bonds and do not contain mass. Under certain conditions, decomposing polyurethane foam produces a char or carbonaceous residue that is thermally stable. In the present report, the formation of thermally stable bonds contributes to char formation.

The δ, d, and g_i represent side-chains or "danglers" in the primary polymer, side-chains or "danglers" in the secondary polymer, and various gas species, respectively. Representative "danglers" are shown boxed in Figs. 4 and 5. Reversible reactions are included to allow the "dan-

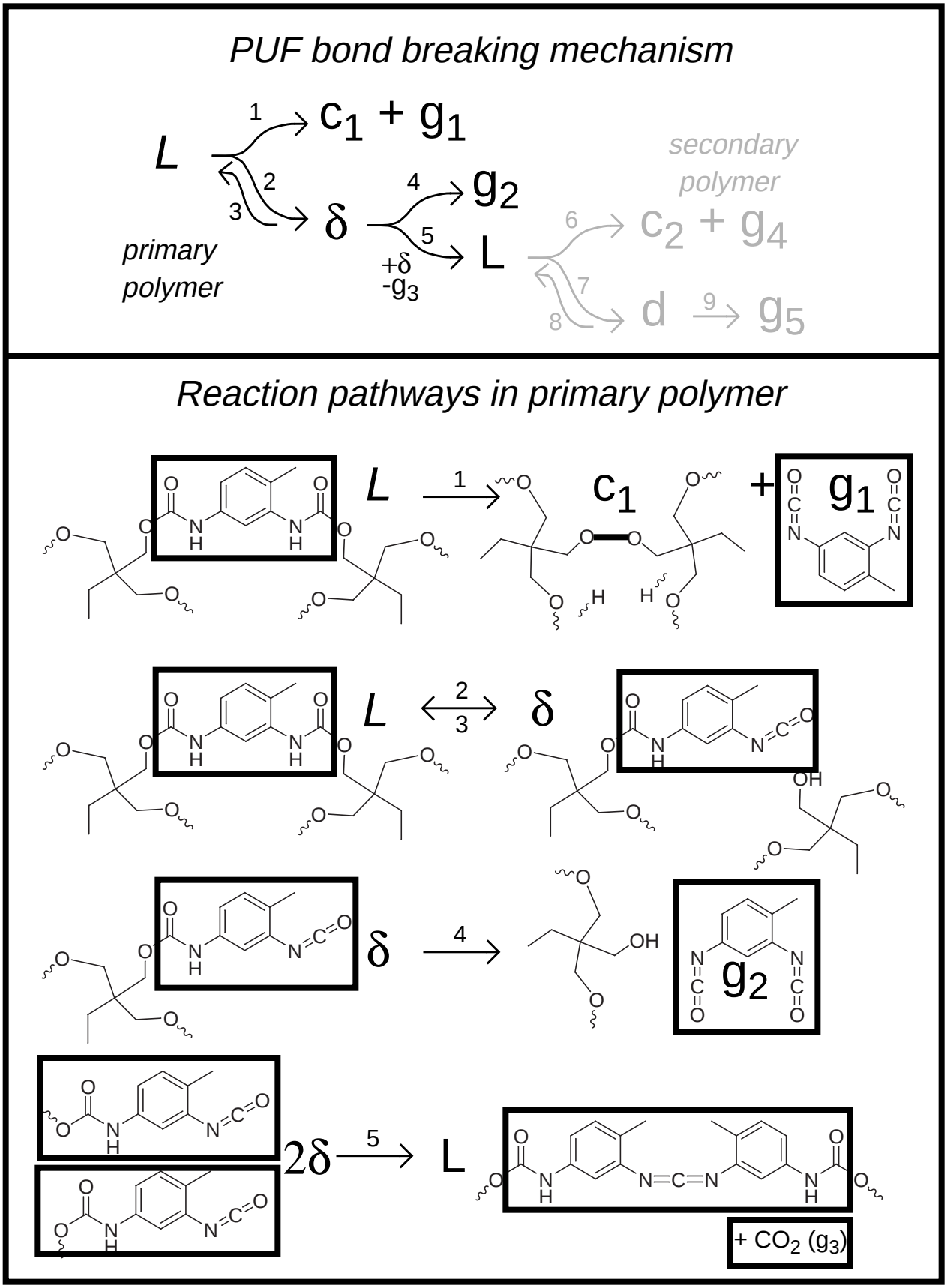

Fig. 4 Kinetic mechanism for decomposition of rigid polyurethane foam with the primary polymer decomposition pathway highlighted.

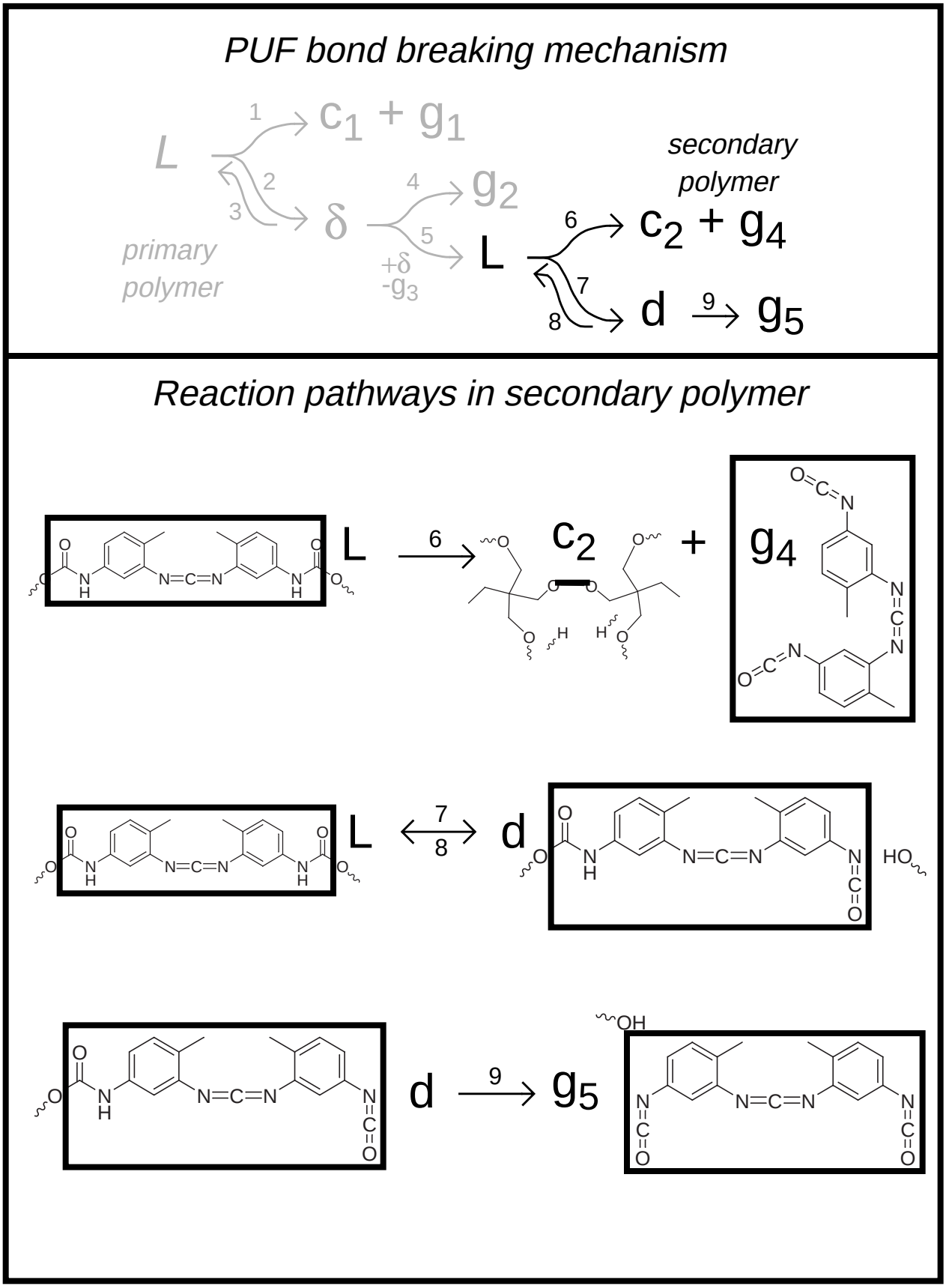

Fig. 5 Kinetic mechanism for decomposition of rigid polyurethane foam with the secondary polymer decomposition pathway highlighted.

glers" to reattach to the polymer. Such reactions will likely be more significant when the foam is degraded under confinement. This nomenclature closely follows Grant et al.[3-5]

The reaction sequence begins when a weak bond - e.g. the ether bond of the carbamate group - is broken to form either a toluene diisocyanate (TDI) side-chain (δ in Fig. 5) or evolves as a gas (g_1 in Fig. 4) with concurrent stabilization of adjacent clusters forming a stable bridge (c_1 in Fig. 4). The TDI side-chains, referred to as danglers, may eventually evolve as light gas fragments (g_2 in Fig. 4) through subsequent, slower reactions. A secondary polymer may evolve as two TDI side-chains react to form a weak bridge (L) with the subsequent evolution of CO_2 denoted as g_3. The molecular weight of L is twice the molecular weight of L minus the molecular weight of g_3. The degradation of the secondary polymer is assumed to be similar to the degradation of the primary polymer except the labile bridge in the secondary polymer has a higher molecular weight.

The proposed mechanism in Figs. 4 and 5 is consistent with preliminary experimental observation. For example, Fig. 6.A shows two bond types that likely break during thermal decomposition: ① the ester bond of the carbamate group and ② the ether bond of the ester group. Experimental evidence of bond type ① breaking is shown in Fig. 6.B, where an IR spectra of decomposition gases obtained using isothermal TGA-FTIR analysis shows an increase in the ~N=C=O stretch region of the IR spectra (wave number of 2250) from evolving gases sampled at 350˚ C, 400˚ C, and 450˚ C. Furthermore, solid-state NMR results, shown in Fig. 6.C, show the depletion of the carbonyls associated with the adipic acid and isocyanate structure. The NMR results are consistent with the bonds labeled ① and ② breaking. Although additional information regarding decomposition chemistry is evident in the NMR data, complete analysis was not avail-

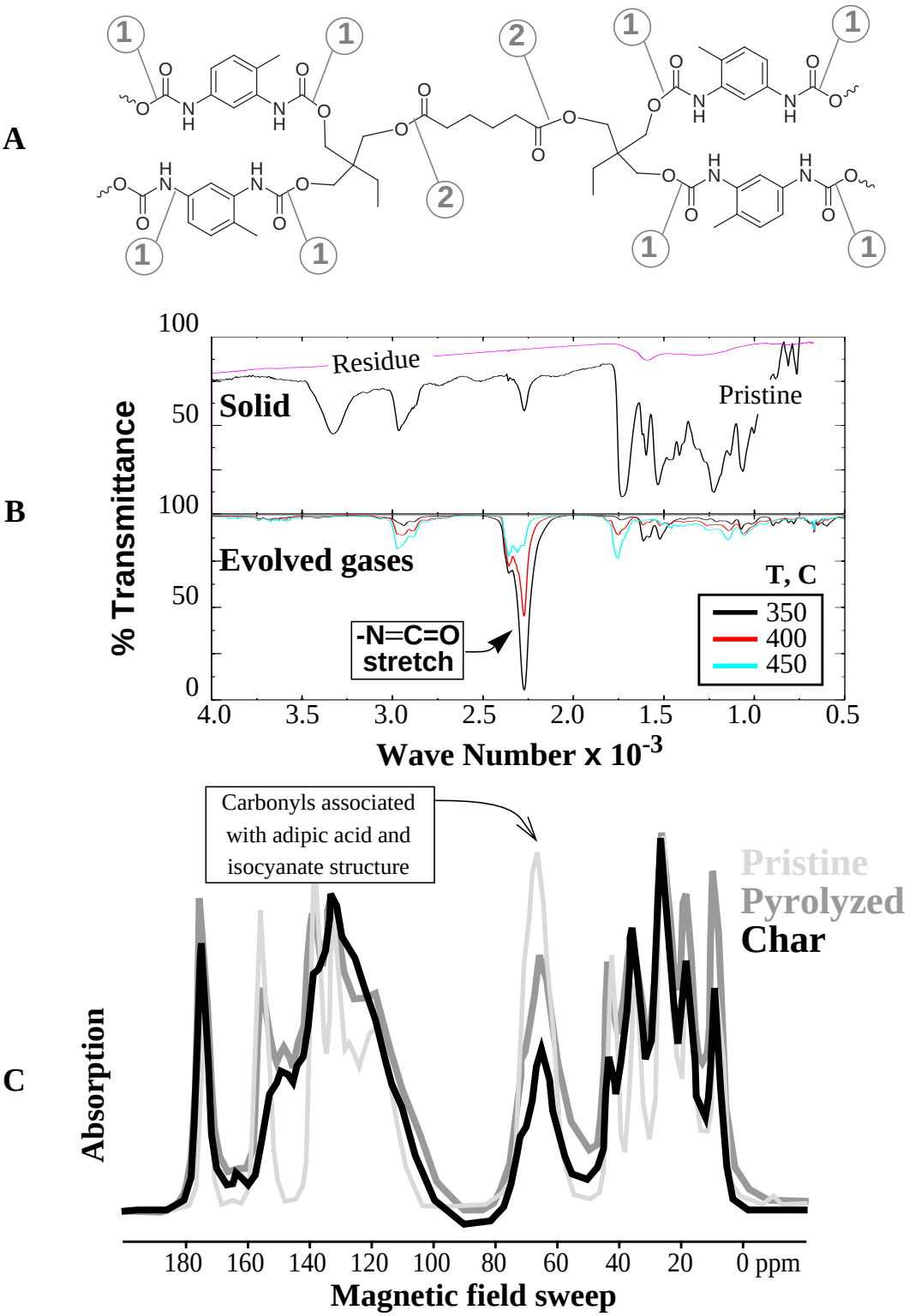

Fig. 6 A) Most probable chemical structure showing two possible weak bonds labeled ① and ②. B) FTIR spectra showing evidence of urethane bond rupture. C) Solid-state NMR evidence showing change in carbonyls associated with adipic acid and isocyanate structures. Other information available in the NMR data has not been fully analyzed.

able because of insufficient funding. The mechanism in Fig. 5 is also consistent with measured decomposition products, such as TDI and trimethoxypropane, as determined from desorption tube analysis.[10]

Table 1 gives the mechanism, rate equations, and initial conditions for the PUF model. The general reaction rate, r_j, for the PUF model bond-breaking scheme is described by:

$$r_j = k_j(T) \prod_{i=1}^{11} N_i^{\mu_{ij}} \quad , \qquad j = 1, \ldots 9 \, , \tag{1}$$

where N_i represents either population parameters L, L, δ, d, c_1, c_2 or species parameters g_1, g_2, g_3, g_4, g_5. The concentration matrix is represented by μ_{ij}, which is given in the footnote of Table 1. The expressions for the kinetic coefficients, $k_j\,(T)$, are given in an Arrhenius form:

$$k_j(T) = A_j \, exp(-E_j / RT) \, , \tag{2}$$

where A_j (1/s), E_j (cal/mol or J/mol), and R (1.987 cal/mol-K or 8.314 J/mol-K) are the pre exponential factors, activation energies, and the universal gas constant, respectively. The species rate of change is given by:

$$dN_i / dt = \sum_{j=1}^{J} \nu_{ij} r_j \quad , \qquad i = 1, \ldots I \, , \tag{3}$$

where ν_{ij} are the stoichiometric coefficients of the jth reaction as given in the footnote of Table 1. The kinetic mechanism requires the Arrhenius parameters, A_j and E_j, to be supplied for each reaction. The initial labile bridge population (L_o) and the initial stable bridge population (c_o) need to be specified as an initial condition. These parameters may represent the extent of polymer curing. The initial value problem described by Eqs. (1)-(3) is solved using DEBDF[11] - a variable order, backward difference, ordinary differential equation solver package.

Table1. Mechanism, rate equations, and initial conditions for the PUF model*

Rxn	Mechanism	Species	Rate Equations	Initial Conditions
		L	$dL/dt = -k_1L - k_2L + k_3\delta$	$L\ (0) = L_o$
(1)	$L \rightarrow c_1 + g_1$	L	$dL/dt = k_5\delta^2 - k_6L - k_7L + k_8L$	L (0) = 0
(2)	$L \rightarrow \delta$	δ	$d\delta/dt = k_2L - k_3\delta - k_4\delta - 2k_5\delta^2$	$\delta\ (0) = 1 - c_o - L_o$
(3)	$\delta \rightarrow L$	d	$dd/dt = k_7L - k_8d - k_9d$	d (0) = 0
(4)	$\delta \rightarrow g_2$	c_1	$dc_1/dt = k_1L$	$c_1\ (0) = c_o$
(5)	$2\,\delta \rightarrow L + g_3$	c_2	$dc_2/dt = k_6L$	$c_2\ (0) = 0$
(6)	$L \rightarrow c_2 + g_4$	g_1	$dg_1/dt = k_1L$	$g_1\ (0) = 0$
(7)	$L \rightarrow d$	g_2	$dg_2/dt = k_4\delta$	$g_2\ (0) = 0$
(8)	$d \rightarrow L$	g_3	$dg_3/dt = k_5\delta^2$	$g_3\ (0) = 0$
(9)	$d \rightarrow g_5$	g_4	$dg_4/dt = k_6L$	$g_4\ (0) = 0$
		g_5	$dg_5/dt = k_9d$	$g_5\ (0) = 0$

* The concentration (μ_{ij}) and stoichiometric matrices (υ_{ij}) with the reactions loaded into 9 columns ($j = 9$) and the species loaded into 11 rows ($i = 11$) are written as:

$$\mu_{ij} = \begin{array}{c} \\ L \\ L \\ \delta \\ d \\ c1 \\ c2 \\ g1 \\ g2 \\ g3 \\ g4 \\ g5 \end{array} \begin{array}{c} \begin{array}{ccccccccc} r_1 & r_2 & r_3 & r_4 & r_5 & r_6 & r_7 & r_8 & r_9 \end{array} \\ \begin{bmatrix} 1 & 1 & 0 & 0 & 0 & 0 & 0 & 0 & 0 \\ 0 & 0 & 0 & 0 & 0 & 1 & 1 & 0 & 0 \\ 0 & 0 & 1 & 1 & 2 & 0 & 0 & 0 & 0 \\ 0 & 0 & 0 & 0 & 0 & 0 & 0 & 1 & 1 \\ 0 & 0 & 0 & 0 & 0 & 0 & 0 & 0 & 0 \\ 0 & 0 & 0 & 0 & 0 & 0 & 0 & 0 & 0 \\ 0 & 0 & 0 & 0 & 0 & 0 & 0 & 0 & 0 \\ 0 & 0 & 0 & 0 & 0 & 0 & 0 & 0 & 0 \\ 0 & 0 & 0 & 0 & 0 & 0 & 0 & 0 & 0 \\ 0 & 0 & 0 & 0 & 0 & 0 & 0 & 0 & 0 \end{bmatrix} \end{array}$$

$$\upsilon_{ij} = \begin{array}{c} \\ dL/dt \\ dL/dt \\ d\delta/dt \\ dd/dt \\ dc1/dt \\ dc2/dt \\ dg1/dt \\ dg2/dt \\ dg3/dt \\ dg4/dt \\ dg5/dt \end{array} \begin{array}{c} \begin{array}{ccccccccc} r_1 & r_2 & r_3 & r_4 & r_5 & r_6 & r_7 & r_8 & r_9 \end{array} \\ \begin{bmatrix} -1 & -1 & +1 & 0 & 0 & 0 & 0 & 0 & 0 \\ 0 & 0 & 0 & 0 & +1 & -1 & -1 & +1 & 0 \\ 0 & +1 & -1 & -1 & -2 & 0 & 0 & 0 & 0 \\ 0 & 0 & 0 & 0 & 0 & 0 & +1 & -1 & -1 \\ +1 & 0 & 0 & 0 & 0 & 0 & 0 & 0 & 0 \\ 0 & 0 & 0 & 0 & 0 & +1 & 0 & 0 & 0 \\ +1 & 0 & 0 & 0 & 0 & 0 & 0 & 0 & 0 \\ 0 & 0 & 0 & +1 & 0 & 0 & 0 & 0 & 0 \\ 0 & 0 & 0 & 0 & +1 & 0 & 0 & 0 & 0 \\ 0 & 0 & 0 & 0 & 0 & +1 & 0 & 0 & 0 \\ 0 & 0 & 0 & 0 & 0 & 0 & 0 & 0 & +1 \end{bmatrix} \end{array}$$

4. STATISTICAL MODEL

Percolation theory, historically applied to describe fluid flow through a network of permeable and impermeable sites, is used to characterize the degraded foam structure with regard to the size and concentration of finite fragments or oligomers. The population variables determined from the kinetic mechanism can be used to determine the fraction of sites that are connected by bridges. For example, the fraction of intact bridges, p, can be determined as follows:

$$p = L + \mathrm{L} + c_1 + c_2 . \tag{4}$$

Percolation theory, using Bethe lattices, is computationally fast, reproducible, and replicates results from more versatile, yet computationally demanding, Monte Carlo methods.[12] Bethe lattices do not contain loop-backs and are similar to tree-like structures. Monte Carlo techniques generate random numbers between 0 and 1 for each bridge. The bridges are either intact (if the random number is between 0 and p) or broken (if the random number is between p and 1). Monte Carlo techniques can be used with realistic chemical structures provided large realizations with many bridges are used to describe the large macromolecules.

One advantage of the Monte Carlo technique over percolation theory is that the polymer fragments can be removed from the network and quenched without affecting the decomposition kinetics of the parent foam structure. If the gas-phase polymer fragments, referred to as oligomers in the present report, are kept at the same temperature as the parent foam, the oligomers thermally crack to form lighter gases and smaller oligomer fragments. The cracking phenomena is properly accounted for using Bethe lattice statistics. In an open system, oligomers do not decompose significantly when cooled to low temperatures and must be accounted for separately as discussed by Kerstein.[13] In the present report, oligomers are assumed to continue to react. This

assumption does not change the prediction of the overall condensed fraction which is used as the criteria for element removal as discussed in Section 7.2.

A detailed formulation of percolation theory based on Bethe lattices is discussed in detail by Grant et al.[3] The mass fraction of finite polymer fragments produced from the thermally degrading foam depends on the population of intact bridges, *p*, determined from the kinetic mechanism and the coordination number, $\sigma + 1$. The lattice statistics are independent of the type of bridges connecting sites provided the bridges can be distinguished as either broken or intact. Thus, percolation theory can be used with any kinetic mechanism provided that the number of broken or intact bridges is determined. A more complex percolation model based on two independent networks has been developed to allow reattachment associated with crosslinking.[12] The "2-σ" model was developed to allow the coordination number of the pristine macromolecule to increase with extent of reaction due to crosslinking.[12] In the current work, the average coordination number does not change with extent of reaction, since the sites are primarily composed of trimethylol propane units. The statistics used for the foam decomposition model in the present report are based on a single coordination number.

Figure 7 shows Bethe lattices with $p = 1$ (all bridges intact), and $p = 0.67$ (67 percent of the bridges intact), for $\sigma + 1 = 2.2$ and $\sigma + 1 = 4$. The smaller coordination number (2.2) is similar to the lattice used by Solomon et al.[14] in a more complex Monte Carlo simulation used to describe lattice statistics. The average coordination number of the three most common structural units shown in Fig. 3 is 2.8.

As the number of broken bridges increases, the fraction of finite polymer fragments increases relative to the fraction of sites belonging to the infinite network. The infinite network no longer exists below a critical bridge population of $1/\sigma$ as shown by Fischer and Essam.[6] The

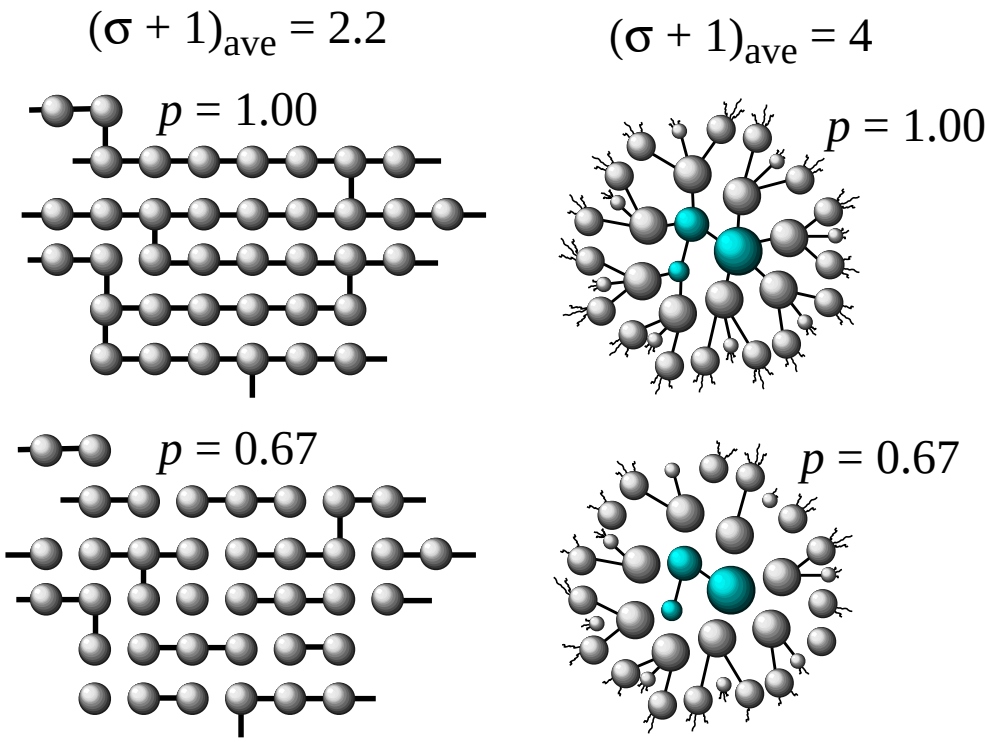

Fig. 7 Bethe lattices with coordination numbers 2.2 and 4.0. Each coordination number example is shown with critical bridge populations of 1.0 and 0.67.

critical bridge populations for the two Bethe lattices shown in Fig. 7 are 0.83 and 0.33 for coordination numbers of 2.2 and 4, respectively. Thus, the $\sigma + 1 = 2.2$ lattice, with $p = 0.67$, is composed of finite polymer fragments exclusively; the higher coordination lattice with $p = 0.67$ still maintains the infinite polymer network.

For Bethe lattices, the number of finite polymer fragments can be determined from the coordination number and the bridge population, p. The probability, F_n, that any given site is a given member of finite polymer fragment of n sites with s bridges is

$$F_n = a_n p^s (1 - p)^\tau, \tag{5}$$

where $$s = n - 1; \tag{6}$$

and $$\tau = n(\sigma - 1) + 2. \tag{7}$$

τ is the number of broken bridges on the perimeter of the polymer fragment with *s*-bridges connecting *n*-sites as shown for the trimer in Fig. 8 The broken bridges isolate the finite polymer fragments from the infinite lattice. Figure 9 shows the weight fraction of various finite polymer fragments as a function of the bridge population for $\sigma = 2$. The number of different ways to form such fragments is represented by a_n:[3]

$$a_n = \left(\frac{\sigma + 1}{n\sigma + 1}\right)\frac{\Gamma(n\sigma + 2)}{\Gamma(n)\Gamma[n(\sigma - 1) + 3]} \tag{8}$$

where Γ represents the standard gamma function.

Equation (5) describes the probability that any given bridge belongs to an *n*-mer. The probability of belonging to an n-mer is the probability that the given bridge is intact or occupied (p^s), multiplied by the probability that the nearest neighbor bridges are broken or unoccupied $(1\text{-}p)^\tau$. a_n accounts for the distinct number of configurations possible for the *n*-mer. Equations (5)-(8) are discussed in more detail in References 3, 6, and 7.

The total fraction contained in all of the finite clusters, *F*, is[3]

$$F = \sum_{n=1}^{\infty} F_n = \left[\frac{1-p}{1-p^*}\right]^{\sigma+1} = \left[\frac{p^*}{p}\right]^{(\sigma+1)/(\sigma-1)}, \tag{9}$$

where p^* is the root of the following equation:

$$z = p^*(1-p^*)^{\sigma-1} = p(1-p)^{\sigma-1}, \text{ or} \tag{10}$$

$$p^*(1-p^*)^{\sigma-1} - p(1-p)^{\sigma-1} = 0; \tag{11}$$

and *p* is determined from Eq. (4). The fraction of sites contained in the infinite cluster, *I*, is

$$I = 1 - F, \tag{12}$$

labeled in Fig. 9 as the infinite cluster, ∞-mer.

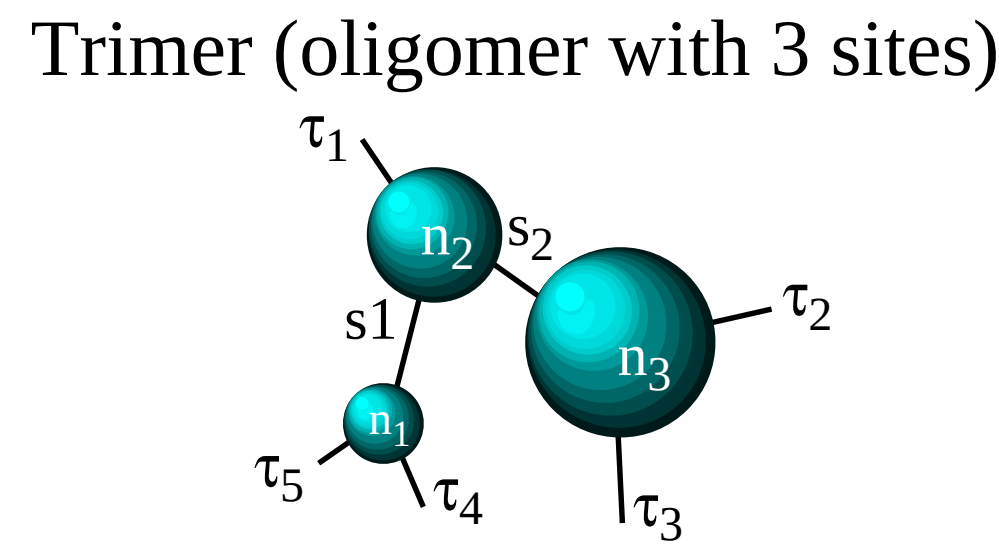

Fig. 8 Trimer showing σ, *n*, *s*, and τ.

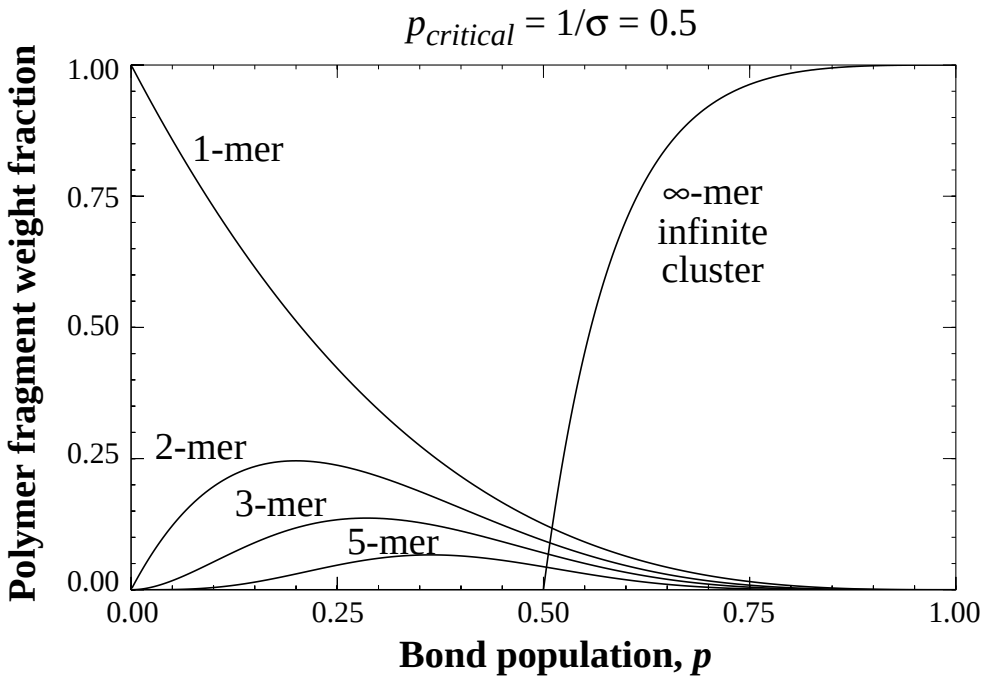

Fig. 9 Weight fraction of finite polymer fragments and the infinite cluster vs. bond population for σ = 2. The curves have been calculated from Eqs. (5) and (12).

For every permissible value of z in Eq. (10), two roots exist in the range $0<p<1$, except at the maximum where the roots are identical as can be seen in Fig. 10. When $\sigma = 2$, z is a simple quadratic function with a maximum at 0.5. A critical bridge population defining the existence of an infinite lattice can be determined by setting the first derivative of z to 0 and solving for p.

$$\frac{dz}{dp} = 0 = (1-\sigma p)(1-p)^{\sigma-2} \Rightarrow p_c = \frac{1}{\sigma} \tag{13}$$

For a cluster to propagate indefinitely from a given intact bridge, the adjoining site must contain at least one other intact bridge. Since p is the probability that a bridge is intact and σ bridges radiate from the adjoining site, an infinite cluster exists only when $\sigma p_c > 1$ or $p_c > 1/\sigma$. The trivial root of Eq. (11), $p^* = p$, should be used when p is less than p_c, making $F = 1$. The other root that is bounded by $0<p^*<p_c$ should be used when p is greater than p_c.

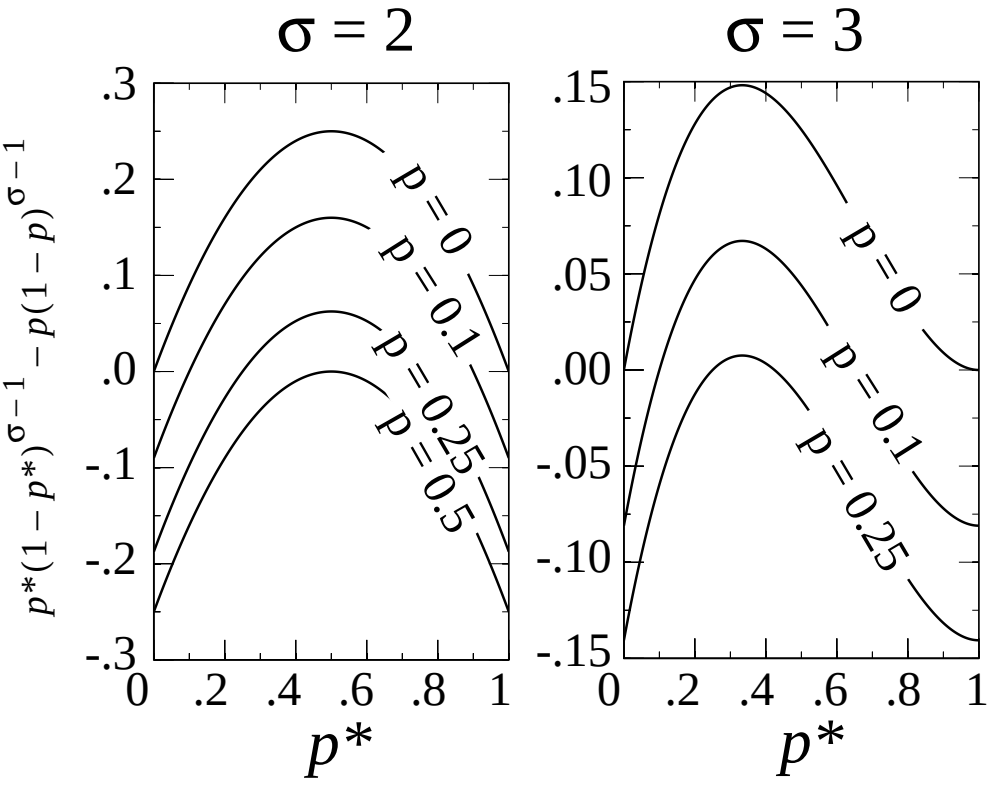

Fig. 10 Plot of Eq. (11) for various σ, p^*, and p.

The mass fraction and molecular weight of each polymer fragment bin can be determined by relating the total mass and mass associated with finite polymer fragments on a site basis. A site is defined as the portion of the polymer that can be isolated by bridges as shown enclosed in dashed lines in Fig.11. The total mass per site is:

$$m_{tot} = M_a + \frac{M_b}{2}(1 - c_o)(\sigma + 1), \tag{14}$$

where M_a is the molecular weight of the site as represented by a sphere (or mer) as shown in Fig. 11, $M_b/2$ is half the molecular weight of the bridges connecting the spheres, and (1-c_o) represents the fraction of bridges which are labile, and σ+1 is the coordination number.

The mass of gas released can also be expressed on a site basis as

$$m_g = \left[\left(\frac{M_b}{2}\right)(g_1 + g_2) + \left(\frac{2M_b - M_{g3}}{2}\right)(g_4 + g_5) + \left(\frac{M_{g3}}{2}\right)(g_3)\right](\sigma + 1), \tag{15}$$

where M_b is the molecular weight of g_1 and g_2, 2 M_b - M_{g3} is the molecular weight of g_4 and g_5, and M_{g3} is the molecular weight of g_3. These molecular weights are divided by two to normalize the gas populations to the total mass per site given in Eq. (14) by noting

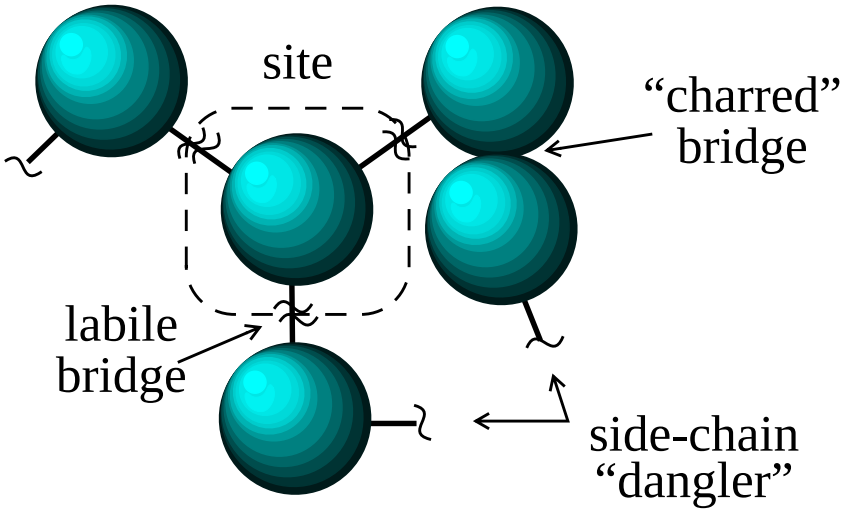

Fig. 11 5-mer showing sites, bonds, and danglers.

$$g_1 + g_2 + g_3 + 2g_4 + 2g_5 \rightarrow (1 - c_o) \qquad \text{as} \qquad \text{time} \rightarrow \infty . \tag{16}$$

The mass of a finite polymer fragment expressed on a site basis, m_n, can be determined from the mass of the finite fragment, M_n, multiplied by the n-site polymer fragment population on a site basis, Q_n:

$$m_n = M_n Q_n \tag{17}$$

where,

$$\boxed{M_n = nM_a + (n-1)M_b\left(\frac{L}{p}\right) + (n-1)(2M_b - M_{g3})\left(\frac{L}{p}\right) + \frac{M_b}{2}\left[\frac{\tau\delta}{(1-p)}\right] + \frac{(2M_b - M_{g3})}{2}\left[\frac{\tau d}{(1-p)}\right]} \tag{18}$$

$$Q_n = F_n / n = b_n p^{n-1}(1-p)^{n(\sigma-1)+2}. \tag{19}$$

M_n is the molecular weight of the n^{th}-polymer fragment bin. Equation (18) and other subsequent boxed equations are primary equations used in the PUF model. The first term in Eq. (18) represents the number of mers in the n-mer multiplied by the mer molecular weight. The second term in Eq. (18) represents the number of bridges, n - 1, in the polymer fragment multiplied by the mass of the bridges of type L. The third term in Eq. (18) represents the number of bridges in the polymer fragment multiplied by the mass of the bridges of type L. The last two terms in Eq. (18) represent the weight of the side-chains, or "danglers," which can evolve over time. The factors $\delta/(1-p)$ and $d/(1-p)$ represent the fraction of side-chains of type δ and d, respectively. The fraction of broken bridges with one side-chain being formed from each broken bridge is represented by (1-p), and τ is the number of bridges that isolate a polymer fragment as given in Eq. (6). The factor "2" in the denominator of the last two terms in Eq (18) is needed to be consistent with Eqs. (14) and (15).

The mass of all finite polymer fragments, m_f, can be determined by summing all of the polymer fragments as follows:

$$m_f = \sum_{n=1}^{\infty} m_n = \sum_{n=1}^{\infty} M_n Q_n . \tag{20}$$

The infinite summation in Eq. (19) can be evaluated by using the following functions derived by Grant et al.:[3]

$$K = \sum_{n=1}^{\infty} Q_n = \left[1 - \left(\frac{\sigma+1}{2}\right)p^*\right]\left[\frac{p^*}{p}\right]^{(\sigma+1)/(\sigma-1)} \tag{21}$$

$$F = \sum_{n=1}^{\infty} nQ_n = \left[\frac{p^*}{p}\right]^{(\sigma+1)/(\sigma-1)} \tag{22}$$

Note that F was defined previously in Eq. (9). Combining Eqs. (6), (18), and (20)-(22) gives

$$\boxed{m_f = M_a F\Phi + M_b K\Omega,} \tag{23}$$

where

$$\Phi = 1 + r\left(\frac{L}{p}\right) + \frac{r\delta(\sigma-1)}{2(1-p)} + \frac{RL}{p} + \frac{Rd(\sigma-1)}{2(1-p)}, \tag{24}$$

$$\Omega = \frac{\delta}{(1-p)} - \left(\frac{L}{p}\right) + \frac{R'd}{(1-p)} - \frac{R'L}{p}, \tag{25}$$

$$r = M_B/M_A, \tag{26}$$

$$R = (2M_B - M_{g3})/M_A, \tag{27}$$

and

$$R' = (2M_B - M_{g3})/M_B. \tag{28}$$

The mass fraction of gas, finite polymer fragments, and infinite lattice can be calculated from Eqs. (14), (15), and (23) as follows:

$$\boxed{f_g = m_g/m_t = \frac{[r(g_1+g_2) + R''g_3 + R(g_4+g_5)](\sigma+1)}{2 + r(1-c_o)(\sigma+1)}} \tag{29}$$

$$f_f = m_f / m_t = \frac{2}{2 + r(1 - c_o)(\sigma + 1)} [\Phi F + \Omega r K] \tag{30}$$

$$f_\infty = 1 - f_g - f_f , \tag{31}$$

where the infinite lattice fraction is referred to as the "gel fraction" by Flory.[7] In Eq. (29), r and R were defined previously in Eqs. (26) and (27), respectively. The variable, R'', represents the ratio of the molecular weight of g_3 to the molecular weight of a site, $R'' = M_{g3}/M_A$. The mass fraction of the finite oligomers, f_f, is the same as given by Grant et al.[3] except for the definitions of Φ and Ω.

The primary variables of interest for the network statistical model are molecular weight of the various gases (M_b is the molecular weight of g_1 and g_2; 2 M_b - M_{g3} is the molecular weight of g_4 and g_5; and M_{g3} is the molecular weight of g3), the mass fraction of the gas (Eq. 29), the molecular weight of the n^{th}-polymer fragment (Eq. 18), and the mass fraction of the n^{th}-polymer fragment. Equation (30) gives the mass fraction of *all* finite fragments. The mass fraction for the *individual* n^{th}-fragments can be determined from Eq. (30) by replacing F and K by nQ_n and Q_n, respectively:

$$\boxed{f_n = \frac{2}{2 + r(1 - c_o)(\sigma + 1)} [\Phi n Q_n + \Omega r Q_n] .} \tag{32}$$

A separate model must be used to determine the amount of finite polymer fragments transported to the gas-phase. The oligomers that are transported into the gas-phase are sometimes referred to as tar.[3,15] Evolution of tar involves condensed-phase diffusion to the surface, vapor-liquid equilibrium at the surface, and diffusion through a gaseous boundary layer. The finite polymer fragments that remain in the condensed phase are sometimes referred to as metaplast.[15] The metaplast (finite polymer fragments) and gel (infinite polymer) are referred to as

char.[15] Ideal vapor-liquid equilibrium is used as a first order approximation to the complex tar diffusion process.

5. VAPOR-LIQUID EQUILIBRIUM MODEL

The fraction of the gaseous oligomers can be determined by using a simple vapor-liquid equilibrium relationship using a combination of Dalton's law and Raoult's law. In the current report, a standard multicomponent isothermal flash calculation was used to determine the split between vapor and condensed phases following the procedure used by Fletcher et al.[5]

In the nineteenth century, Dalton observed that the pressure exerted by a mixture of ideal gases is the same as the sum of pressure exerted by the individual gases occupying the same volume.[16] Dalton's law states that the partial pressure is the gas-phase mole fraction, y_i, multiplied by the total pressure, P:

$$P_i = y_i P . \tag{33}$$

Raoult observed that the partial pressure in the vapor, P_i, of each component in an ideal liquid solution was proportional to the components mole fraction in the liquid, x_i, with the proportionality constant being the vapor pressure of the pure component at the system pressure, P^*:[17]

$$P_i = P_i^* x_i . \tag{34}$$

Ideal solutions with chemically similar components obey Raoult's law, and dissimilar species deviate strongly from Raoult's law. Eqs. (33) and (34) can be combined to define a "K-value" or vapor-liquid equilibrium ratio:[17]

$$K_i = \frac{y_i}{x_i} = \frac{P^*}{P}. \tag{35}$$

A standard *multicomponent isothermal flash calculation*[17] can be used with Eq. (35) to determine the split between vapor and liquid. A mole balance between the initial condensed phase, *F*, and the resulting vapor phase, *V*, and liquid phase, *L*, is

$$F = V + L, \tag{36}$$

where *F*, *V*, and *L* refer to total moles of feed, vapor, and liquid, respectively. The feed in the PUF decomposition model includes the sum of the finite polymer fractions determined from percolation theory on a mole basis determined from Eqs. (18) and (32). The feed also includes the gases g_1 through g_5 that are calculated with the kinetic mechanism. The moles of the individual components in the feed, f_i, vapor, v_i, and liquid l_i, sum to *F*, *V*, and *L*, respectively:

$$F = \sum_{i=1}^{n} f_i,\ V = \sum_{i=1}^{n} v_i, \text{ and } L = \sum_{i=1}^{n} l_i \tag{37}$$

$$f_i = z_i F,\ v_i = y_i V, \text{ and } l_i = x_i L. \tag{38}$$

z_i, y_i, and x_i represent the mole fraction of the i^{th} component in the feed, vapor, and liquid, respectively. An expression for x_i can be determined from a single component material balance:

$$f_i = v_i + l_i \tag{39}$$

$$z_i F = K_i x_i V + x_i L = K_i x_i V + x_i [F - V] = x_i (F - V + K_i V), \tag{40}$$

$$\text{or } x_i = \frac{z_i F}{(F - V + K_i V)} = \frac{z_i}{\left(1 - \frac{V}{F} + \frac{K_i V}{F}\right)} = \frac{z_i}{(K_i - 1)\frac{V}{F} + 1}. \tag{41}$$

An expression of y_i can be determined from Eqs. (35) and (41) as

$$y_i = K_i x_i = \frac{K_i z_i}{(K_i - 1)\frac{V}{F} + 1}. \tag{42}$$

A stable implicit equation to solve for *V*/F can be determined using the identity $\Sigma\, x_i = \Sigma\, y_i = 1$, or

$$\sum_{i=1}^{n} y_i - \sum_{i=1}^{n} x_i = 0 = \sum_{i=1}^{n} \frac{K_i z_i}{(K_i - 1)\frac{V}{F} + 1} - \sum_{i=1}^{n} \frac{z_i}{(K_i - 1)\frac{V}{F} + 1}, \tag{43}$$

$$\text{or } 0 = \sum_{i=1}^{n} \frac{z_i (K_i - 1)}{(K_i - 1)\frac{V}{F} + 1}. \tag{44}$$

V/*F* is determined iteratively using the *zeroin* solver.[18] Eq. (44) is the Rachford-Rice equation.[17]

The gases g_1 through g_5 must be combined with the finite fragments to calculate the feed mole fractions, z_i. The "K-values" defined in Eq. (35) can be determined from the vapor pressure of the pure components, *P**, divided by the system pressure, *P*. Fletcher et al.[5] have proposed the following vapor pressure correlation for high molecular weight organic molecules:

$$P_n^* = 87100 \exp\left(\frac{-299 M_n^{0.590}}{T}\right), \tag{45}$$

where P_n^* is the vapor pressure of the pure n^{th}-polymer fragment in atmospheres, M_n is the molecular weight of the n^{th}-polymer fragment in g/mol as determined from Eq. (18), and *T* is the temperature in K. The coefficients in Eq. (45) were obtained from coal tars with molecular weights ranging from 110 to 315 amu. The vapor pressure predicted with Eq. (45) increases with lower molecular weight species. The functional form of Eq. (45) is similar to the Clausius-Clapeyron equation which is usually used to determine the vapor pressure at any temperature when the vapor pressure is known at another temperature:

$$P^* = P^*_{known} \exp\left[\frac{-\Delta H_v}{R}\left(\frac{1}{T} - \frac{1}{T_{known}}\right)\right], \quad (46)$$

where ΔH_v is the molar heat of vaporization and R is the gas constant.

Fletcher et al.[5] have shown acceptable agreement with boiling point data for 111 organic compounds at pressures of 0.007, 0.08, 1, and 10 atm using the correlation given in Eq. (45). The 111 organic compounds, with molecular weights as high as 244, did not contain long chain alkanes or compounds with more than two oxygen atoms. Long chain hydrocarbons are not expected to occur in the polyurethane tar in significant quantities. However, some of the expected products measured by Chu et al.,[10] such as trimethoxypropane, do contain more than two oxygen atoms.

The vapor pressures of expected polyurethane decomposition products, such as alcohols, acids, esters, and isocyanates, are likely to behave according to the correlation in Eq. (45) within each family of products. The most prevalent decomposition products are TDI (see g_1 and g_2 in Fig. 4) and carbon dioxide (CO_2). In the current work, specific vapor pressure correlations for TDI and CO_2 were used rather than the correlation in Eq. (46). Specifically, the TDI vapor pressure was used for g_1 and g_2; the CO_2 vapor pressure was used for g_3; and the correlation given in Eq. (45) was used for g_4, g_5, and the polymer fragments determined from percolation theory. More experiments are needed to improve the vapor pressure correlation for polyurethane foam fragments.

6. ESTIMATING THE PUF DECOMPOSITION MODEL PARAMETERS

Nominal values of the parameters used in the PUF model are shown in Table 2 with an estimate of the high and low values used in the sensitivity analysis discussed in Section 7.1. The initial bridge

population parameters, p_o and c_o, were estimated based on the degree of polymer curing. The coordination number and molecular weights were calculated from the three most common structural units of the foam as shown in Figs. 2 and 3. Figure 3 shows sites made from the trimethylol propane units and the diethylene glycol units. The bridges are composed of TDI and adipic acid structures. Table 3 shows how the average molecular weights and coordination numbers for the 60%, 20%, and 10% most probable structural units were calculated. The molecular weights and coordination number in Table 2 were determined by taking the probability normalized molecular weights and coordination numbers from Table 3 as follows:

$$M_a = \frac{0.6}{0.9}(131) + \frac{0.2}{0.9}(118) + \frac{0.1}{0.9}(104) = 125 \text{ g/mol} \tag{47}$$

$$M_b = \frac{0.6}{0.9}(163) + \frac{0.2}{0.9}(160) + \frac{0.1}{0.9}(155) = 161 \text{ g/mol} \tag{48}$$

$$\sigma + 1 = \frac{0.6}{0.9}(3) + \frac{0.2}{0.9}(2.5) + \frac{0.1}{0.9}(2) = 2.8\,. \tag{49}$$

The Arrhenius parameters were obtained by minimizing the root mean squared error between the calculated and measured mass loss for six, unconfined, isothermal TGA experiments using DAKOTA (Design Analysis Kit for OpTimizAtion, Ref. 20). The unconfined TGA experiments considered nominally 5-mg samples in open platinum pans and were designed to examine decomposition mechanisms under conditions that minimize mass transfer and reversible and secondary reactions.[10,21] Figures 12.A and 12.B show a comparison between predicted and measured condensed mass fractions (foam mass measured by the TGA divided by the initial foam mass) for the isothermal TGA experiments used to obtain the kinetic parameters. The single isothermal TGA samples were quickly ramped (~10-15 min) to the temperatures indicated in Fig. 12.A. The dual isothermal TGA samples were ramped to 300˚ C and held for about two hours, then ramped to the temperatures indicated in Fig. 12.B. The three single isothermal experiments

Table 2. PUF model parameters with estimated values for sensitivity analysis*

Variable Symbol	Description	Nominal Value	Low Value (+)	High Value (-)
P_o	Initial bond population†	0.85	0.8	0.9
c_o	Initial strong bond population†	0.10	0.05	0.15
$\sigma+1$	Coordination number‡	2.8	2.1	3.0
M_c	Site molecular weight‡	125 g/mol	104 g/mol	131 g/mol
M_b	Bridge molecular weight‡	161 g/mol	155 g/mol	163 g/mol
M_{g3}	Molecular weight of g_3‡	44 g/mol	44 g/mol	44 g/mol
P	Pressure†	83 KPa	82 KPa	84 KPa
E_1	Activation Energy for reaction 1†	53400. cal/mol	$0.9\times E_1$	$1.1\times E_1$
E_2	Activation Energy for reaction 2†	44580. cal/mol	$0.9\times E_2$	$1.1\times E_2$
E_3	Activation Energy for reaction 3†	42520. cal/mol	$0.9\times E_3$	$1.1\times E_3$
E_4	Activation Energy for reaction 4†	45900. cal/mol	$0.9\times E_4$	$1.1\times E_4$
E_5	Activation Energy for reaction 5†	44600. cal/mol	$0.9\times E_5$	$1.1\times E_5$
E_6	Activation Energy for reaction 6†	58060. cal/mol	$0.9\times E_6$	$1.1\times E_6$
E_7	Activation Energy for reaction 7†	51850. cal/mol	$0.9\times E_7$	$1.1\times E_7$
E_8	Activation Energy for reaction 8†	52830. cal/mol	$0.9\times E_8$	$1.1\times E_8$
E_9	Activation Energy for reaction 9†	56660. cal/mol	$0.9\times E_9$	$1.1\times E_9$

* All frequency factors, *A*, were assumed to be equal to $3.0\text{x}10^{15}$ s^{-1}.
† High and low values guessed.
‡ High and low values from the 10% and 60% most probable chemical structure.

Table 3. Molecular weight and coordination number of common foam structural units

Structure*	M_a, g/moll	M_b, g/mol	$\sigma + 1$
60% most probable	131	[(4×176) + 112]/5 = 163	3
20% most probable	(104+131)/2 = 118	[(3×176) + 112]/4 = 160	(2 + 3)/2 = 2.5
10% most probable	104	[(2×176) + 112]/3 = 155	2

* See Fig. 3 for the boundaries used to decompose the most probable structural units into bridges used to determine M_B and sites used to determine M_A as well as $\sigma + 1$.

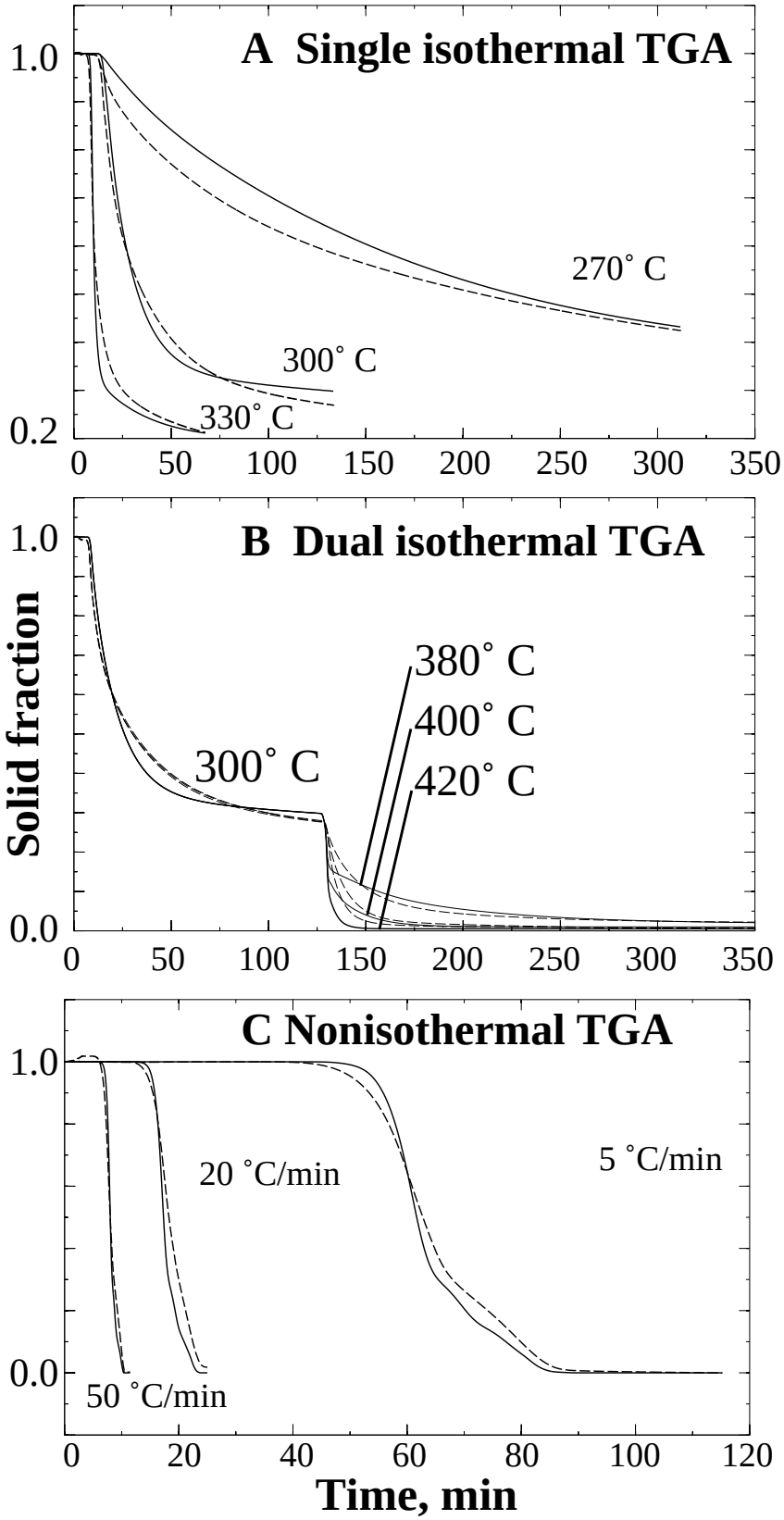

Fig. 12 Comparison of PUF predicted (solid line) and measured (dashed line) solid mass fraction for A) single isothermal TGA, B) dual isothermal TGA, and C) three nonisothermal TGA experiments.

shown in Fig. 12.A were intended to isolate the kinetics for the decomposition of the initial polymer and formation of the secondary polymer as discussed in more detail by Erickson et al.[21] The final three isothermal experiments shown in Fig. 12.B were ramped to 300˚ C and held until mass loss was minimal and then ramped to the final isothermal temperature of 380˚ C, 400˚ C, and 420˚ C, respectively. The intent of these final three experiments was to isolate the kinetics of the decomposition of the secondary polymer.

The predicted solid fraction is greater than the measured solid fraction for the 270˚ C isothermal TGA results shown in Fig. 12.A. The difference between the predicted and measured solid fraction is not as pronounced at 300˚ C and 330˚ C. At the lower temperature, alternate reaction pathways involving evolution of a site, such as a trimethylol propane with subsequent crosslinking of the resulting urethane danglers, may explain the differences. Future work will address this issue.

The kinetic parameters, determined from the six isothermal TGA experiments, are given in Table 2. Three nonisothermal experiments, not used to estimate kinetic parameters, were simulated to validate the selection of the kinetic parameters for the PUF model. Fig. 12.C shows good agreement between predicted and measured condensed mass fraction for the three nonisothermal TGA experiments with heating rates of 5, 20, and 50 ˚C/min.

Figure 13 shows the predicted solid fraction and measured solid fraction for the 20 ˚C/min TGA case for a 4.687-mg sample and a 13.765-mg sample. Differences in the experimental results are probably related to mass transport effects. However, both sets of data show an initial rapid decomposition followed by a slower rate of solid mass loss.

Figure 14 shows solid mass fraction, population parameters, the gas and oligomer mass fractions, and gas molecular weight for the 5 ˚C/min ramped TGA experiment. Between 0 and 40

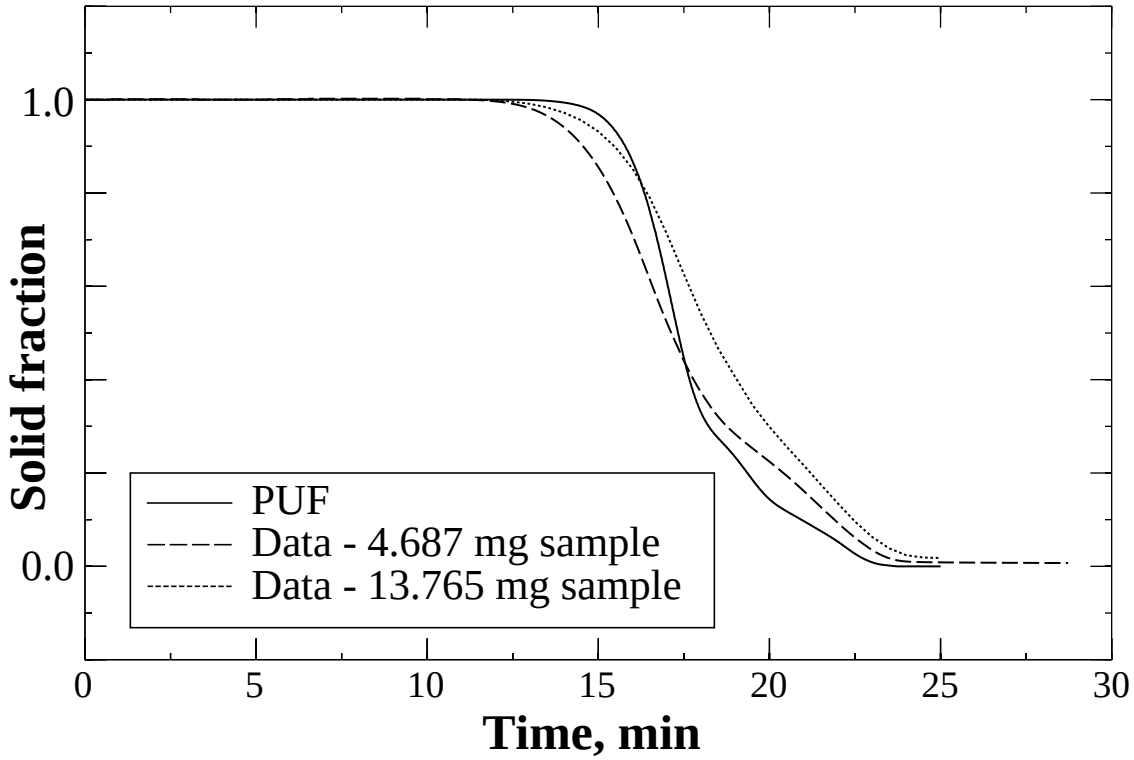

Fig. 13 Comparison of PUF predicted (solid line) and measured (dashed and dotted lines) solid mass fraction for the 20 ˚C/min TGA experiment. The dashed lines are for a 4.687-mg sample, and the dotted line is for a 13.765-mg sample.

minutes in Fig. 14.B, P is shown to be the sum of L and c_1. At 40 minutes, δ starts to decrease with a corresponding increase in L, a result of side-chain cross-linking of δ to form the bridge L. At 50 minutes, the secondary bridge, L, begins to form as a result of reaction between two δ side-chains. The increase in both L and L causes the bridge population, p, to increase between 40 and 50 minutes. Decay of the weak bridge, L, is shown as the side-chain population δ increases. The strong bridge formation in the primary and secondary polymer are minimal. However, the formation of strong bridges may become significant at elevated pressures.

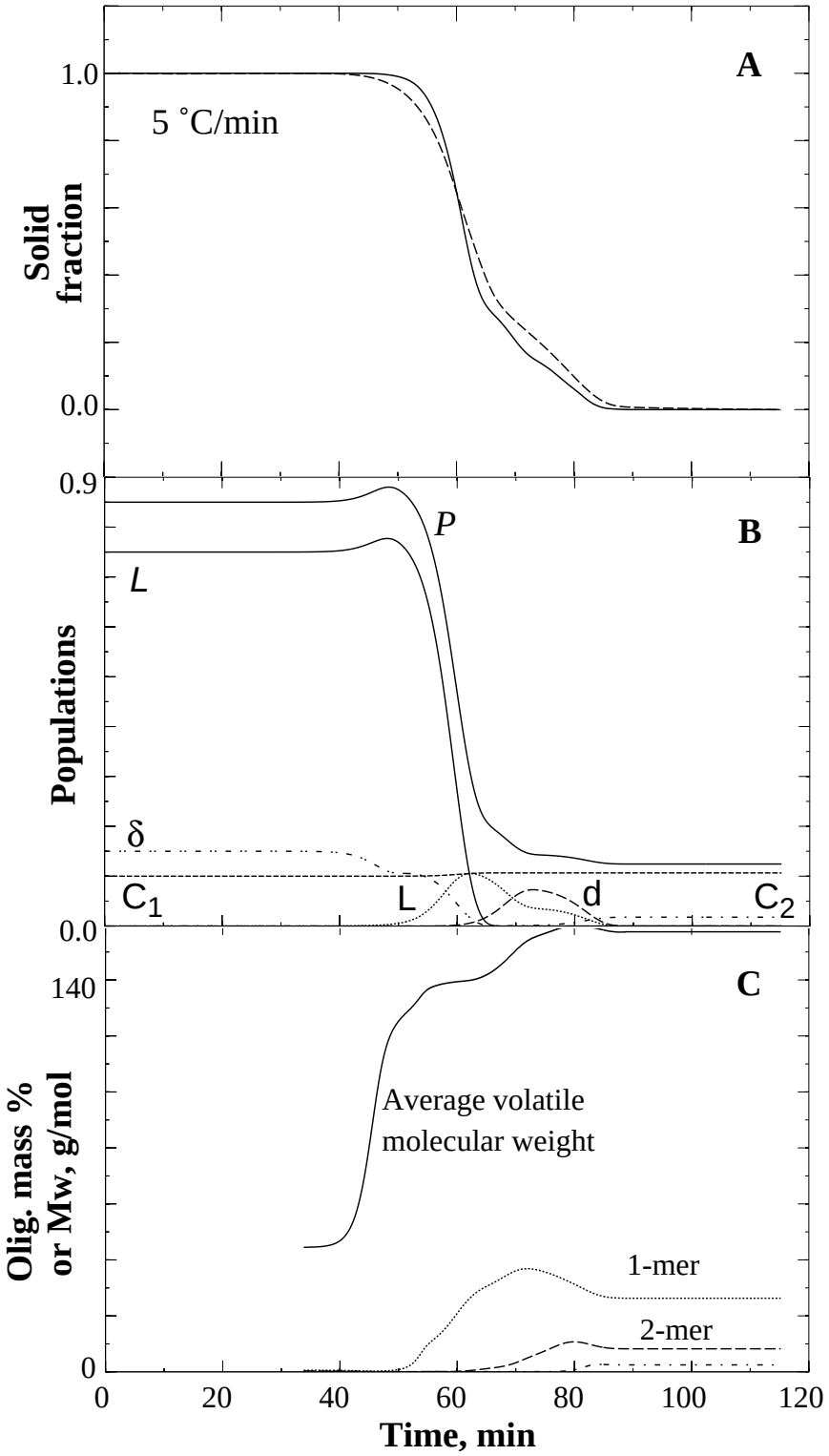

Fig. 14 A) Comparison of PUF predicted (solid line) and measured (dashed line) solid mass fraction for a 5 ˚C/min TGA experiment. B) Predicted population parameters for the 5 ˚C/min TGA experiment given in A. C) Predicted average volatile molecular weight and various oligomer mass percents for the 5 ˚C/min TGA experiment given in A.

7. UNCERTAINTY AND SENSITIVITY ANALYSIS OF THE PUF MODEL

Two techniques were used to analyze parameters in the decomposition model: 1) a variance analysis discussed in Section 7.1 and 2) a response derivative analysis discussed in Section7.3. A grid refinement analysis is also reported in Section 7.2 to establish that solutions are not dependent on the size of elements used in the simulations.

The variance analysis is used to examine primary PUF model parameters that effect the prediction of condensed mass fraction for the 20 ˚C/min ramped TGA experiment. Parameters with primary effects were the initial bridge population, P_o; the lattice coordination number, σ+1; molecular weight of the bridging structures, Mw_b; and several activation energies associated with the formation of a secondary polymer, E_i.

Two response derivative analysis are performed for fast (0.97±0.14 cm/min) and slow (0.26±0.05 cm/min) recession rate conditions. For the fast recession rate analysis, the most sensitive parameters are the activation energies associated with the formation of the secondary polymer. For the slow recession rate analysis, the most sensitive parameters are associated with the thermophysical properties of the foam and the destruction of the secondary polymer.

7.1 VARIANCE ANALYSIS

To determine the primary effects of various PUF model parameters, a simple sensitivity analysis is performed on 15 parameters using a two-level 20-run Plackett Burman[22] analysis. Typically, Plackett Burman analyses are used in experimental design techniques. These techniques are also useful in determining parameter sensitivity. Primary effects are determined by comparing calcu-

lated factor effects with probability points of a 2-sided t-distribution with 4 degrees of freedom. One degree of freedom is used to estimate the mean. The primary response variable for this study is chosen to be the condensed fraction remaining during decomposition of polyurethane foam ramped at 20 ˚C/min as in the thermogravimetric analysis (TGA). The 15 parameters used for this study are given in Table 2. The sensitivity of M_{g3} was not determined, since g_3 is assumed to be CO_2. The 20-run Plackett Burman design used in this study is given in Ref. 22.

To determine significant factor effects using Plackett Burman analyses, a low value and high value for each of the PUF variables are selected as shown in Table 2. Some of the values are arbitrarily chosen. For example, the high and low values for the activation energies are taken as the nominal value ±10%. The molecular weight values are taken from the 10% and 60% most probable structures. Twenty simulations of the TGA experiment with a 20 ˚C/min. ramp are run with the parameters set to either the low value or the high value as described in Ref. 22. The condensed mass fraction at various times is used as the response variable. From the response at these times, a factor effect is calculated using methods discussed in Ref. 22. The significant factors based on a 90% confidence interval are shaded and boxed in Table 4. The factor effects before 480 seconds are zero, since the temperature is below significant reaction thresholds. Additional information regarding statistical inference using Plackett Burman analysis can be found in Reference 22.

The Plackett Burman analyses indicate that the three structural parameters, P_o, σ+1, and M_b, are significant in the early decomposition phase, since the significant factor effects are only present in the early stages of mass loss between 480 and 780 seconds. These results are dependent on the selection of the low and high values of each parameter. The parameters with a small difference between the high and low values, such as pressure, are shown to have small factor

Table 4. Calculated factor effects from Plackett Burman Analysis*

Time, s	P_0	c_0	σ+1	M_c	M_b	P	E_1	E_2	E_3	E_4	E_5	E_6	E_7	E_8	E_9
480	1.25	0.57	**-3.18†**	0.37	0.75	-0.75	-0.12	-0.82	-0.80	0.62	**3.18†**	-0.80	0.37	-0.82	-1.25
540	**2.29†**	0.69	**-3.34†**	-0.20	1.06	-1.06	0.47	-0.96	-1.13	0.76	**3.34†**	-1.13	-0.20	-0.96	**-2.29†**
600	**4.41†**	0.83	**-2.30†**	-0.58	**2.52†**	0.32	0.59	0.78	-0.37	1.40	**7.59†**	-1.55	-0.59	-0.64	-1.70
660	**2.59†**	1.23	**-2.69†**	-1.02	0.51	0.39	-0.16	1.23	-1.32	**2.42†**	**5.48†**	-1.19	-0.73	0.61	-1.92
720	0.29	0.82	**-2.35†**	-0.55	-0.31	-0.29	-1.71	**3.16†**	**-3.31†**	**2.58†**	**4.65†**	-1.97	0.42	**2.97†**	-1.16
780	-0.92	1.00	**-2.77†**	0.45	-0.95	-0.48	-1.94	**4.43†**	**-3.25†**	**3.56†**	**4.06†**	**-2.80†**	0.42	**3.44†**	0.06
840	-0.64	1.08	-0.10	0.66	0.34	-1.40	-0.40	**3.94†**	-0.19	**4.19†**	1.20	-0.68	0.84	1.16	0.96
900	-0.80	0.60	0.26	0.48	0.38	-1.12	0.17	**2.62†**	1.02	**2.75†**	-0.04	-0.10	0.53	-0.15	0.71
960	-0.75	0.33	0.34	0.47	0.48	-1.04	0.42	**2.41†**	1.09	**3.02†**	0.03	-0.11	0.58	-0.15	0.72
1020	-0.93	0.03	0.80	0.73	0.82	-0.91	1.68	2.10	0.93	**4.13†**	-0.10	-0.51	0.28	-0.47	0.56
1080	-0.89	-0.69	1.59	0.40	-0.19	-0.89	**2.25†**	0.89	0.19	**5.96†**	-0.02	-0.26	0.27	-1.23	0.56
1140	-0.46	-1.19	1.14	-0.04	-1.38	-0.27	1.73	1.02	-0.98	**5.06†**	-0.49	0.55	0.68	-1.50	0.99
1200	-0.39	-1.25	0.18	0.00	-1.44	-0.01	0.90	1.20	-1.10	**3.53†**	-0.90	1.02	0.31	-0.64	1.00
1260	-0.42	-0.87	-0.22	-0.11	-1.07	0.08	0.29	1.00	-1.01	**2.15†**	-1.10	1.27	-0.15	-0.05	0.84
1320	-0.51	-0.81	-0.05	-0.17	-1.03	0.20	0.20	1.24	-1.09	1.91	-1.13	1.37	-0.22	-0.12	0.92
1380	-0.45	-0.90	0.45	-0.15	-0.78	0.68	-0.25	1.81	-0.89	1.49	-1.14	1.29	-0.44	-0.63	1.38
1440	-0.51	-0.70	0.94	0.31	-0.75	1.18	-1.02	**2.26†**	-0.65	1.06	-1.46	1.51	-0.28	-1.15	1.94
1500	-0.59	-0.39	1.23	0.85	-0.71	1.45	-1.43	**2.64†**	-0.82	0.79	-1.85	1.65	-0.12	-1.48	2.09

* Confidence interval (double-sided probability point of t-distribution): 80% (1.33) 90% (2.13) 95% (2.78) 98% (3.75) 99% (4.60)

†Significant factor effects based on 90% confidence interval using four degrees of freedom.

effects. If the difference between the high and low values were greater, the factor effect may have been more significant. Specification of the initial bridge population, P_o, is more significant than specification of the initial strong bridge population, c_o, as shown in Table 4. The lattice coordination number, $\sigma+1$, and the molecular weight of bridges are also significant factors that describe the chemical structure of the foam.

The Plackett Burman analysis also shows that all of the steps in the bond-breaking scheme are significant except for Reaction (7) in Table 1. The analysis also indicates that the most sensitive pathway is the formation of the secondary polymer. At the expense of losing generality, the PUF model could possibly be simplified for the 20 ˚C/min TGA simulation.

7.2 GRID-INDEPENDENT SOLUTIONS USING FINITE ELEMENT ANALYSIS

Calculation of the object function for the response derivative analysis discussed in Section 7.3 requires grid-independent solutions using a finite element heat conduction code. The PUF decomposition model is implemented into the finite element heat transfer code, COYOTE,[1] employing a user subroutine. COYOTE is a two- or three- dimensional, finite element, massively parallelized computer program designed for analysis of nonlinear heat conduction problems. In addition to solving standard thermal diffusion problems, COYOTE includes the effect of phase change, condensed-phase chemistry, and surface-to-surface radiation. Material deletion is included through the use of the finite element "death" capability. Elements can be removed to create a "dynamic" radiation enclosure. Viewfactors are recalculated whenever an element dies. Gaps at material interfaces are modeled as contact surfaces. Material properties can be temperature and/or species dependent and either isotropic or orthotropic. A wide variety of boundary

conditions are supported in COYOTE, and pre and postprocessing file formats are used which permit integration with existing meshing and graphics visualization programs. For the simulations reported in the current work, elements are dynamically removed from the simulation when the condensed fraction within an element dropped below 1%. The velocity of the decomposition front, referred to as the burn front in this report, is determined from the time of element death. In The decomposition front is referred to as a "burn front" since burning is defined as material destruction by heat. The foam recession rate is referred to in this report as the foam "burn rate."

The one-dimensional simulation of burning foam was performed with COYOTE using a single column of elements as shown on the left side of Fig. 15. Three sides of the column of elements were assumed to be insulated and the fourth side was exposed to various boundary conditions such as radiation. Experimentally determined[23] thermal conductivity and specific heat were used in the one-dimensional simulations. Several methods can be used to determine the grid sensitivity of decomposing polyurethane foam. For example, the size of the element can be reduced until there is no change in the burn front velocity as shown in the plot of Fig. 15. Another method would be to specify a sufficient number of elements across the reaction front to resolve steep gradients in temperature or species profiles.

The grid error in the legend of Fig. 15 is defined as

$$\text{grid error} = 100 \times (V_i - V)/V_i, \tag{50}$$

where V represents the burn velocity and V_i represents the grid-independent burn velocity. The grid-independent foam recession rate in Fig. 15 is 1.14 cm/min. Figure 16 shows the grid error for a one-dimensional model with two separate constant flux boundary conditions. The grid-inde-

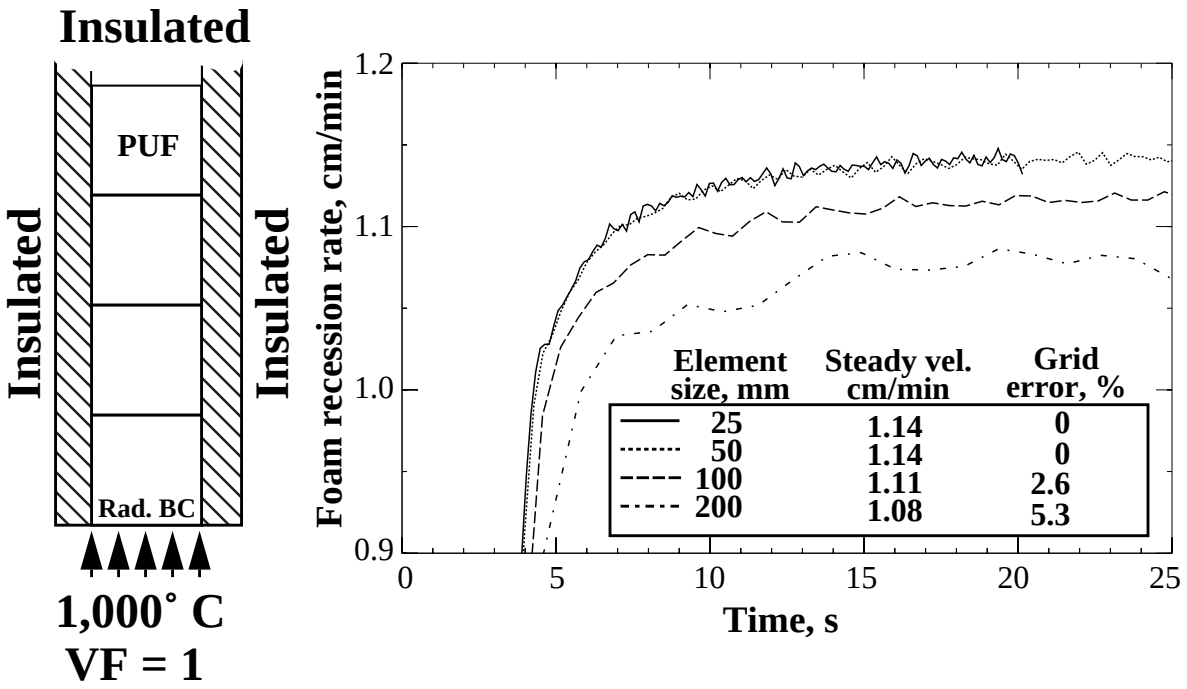

Fig. 15 Dependence of foam recession rate on element size for a one-dimensional model with a radiative boundary condition.

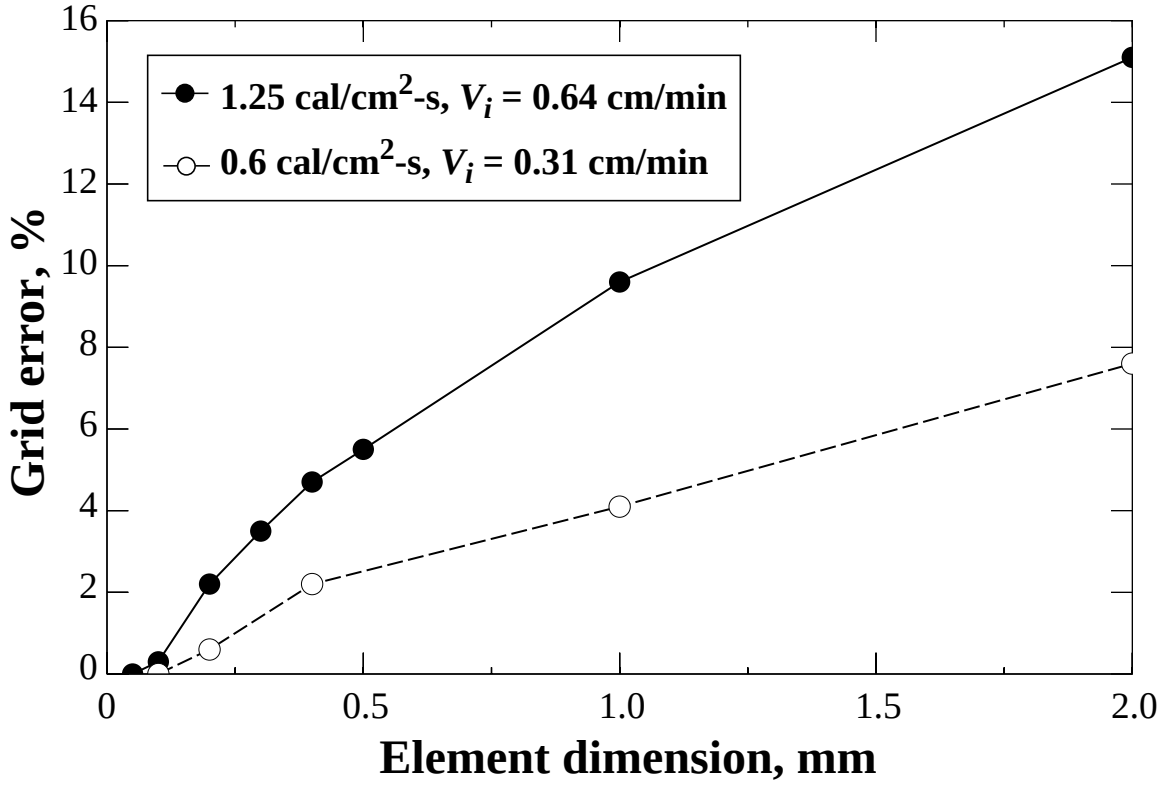

Fig. 16 Grid error calculated from Eq. (50) for a one-dimensional model with flux boundary conditions.

pendent foam recession rate, V_i, is equal to 0.64 cm/min and 0.31 cm/min for the 1.25 cal/cm^2-s and 0.6 cal/cm^2-s boundary conditions, respectively.

In Fig. 16, the predicted velocity using 2-mm grids is 0.54 cm/min, giving a grid error of 15% for the 1.25 cal/cm^2-s case. Simulations using elements smaller than 2-mm predict faster burn rates than 0.54 cm/min. The faster burn rates for the simulations using smaller elements is related to element death. For example, in the simulations using smaller elements, the criteria for element removal, condensed fraction being less than 0.01, is satisfied earlier than the criteria would be satisfied for a simulation using larger elements. The smaller elements are removed from the computational domain, and the boundary condition is then applied to the newly exposed element. For an element size of 0.5-mm, the grid error is less than five percent. The temperature gradient across each element is also an indication of when grid independence is achieved. For example, grid independence in the present study was achieved when the temperature gradient across a dying element was approximately 50 ˚C or less. Three-dimensional calculations, using 0.05-mm elements are currently not practical without adaptive gridding. However, 0.5-mm elements, can be used with some expense.

7.3 RESPONSE DERIVATIVE ANALYSIS

The object oriented optimization code, DAKOTA,[20] used to determine the PUF model activation energies, can also be used to determine the gradient of an object function with respect to model parameters. This response derivative can be used to quantitatively determine the uncertainty in predicted results. In this report, two response derivative analysis were performed for fast (0.97±0.14 cm/min) and slow (0.26±0.05 cm/min) burning conditions. For the response derivative analysis, the object function was chosen to be the steady-state foam recession rate for

one-dimensional foam decomposition, as discussed in Section 7.2. The TGA simulations, discussed in Section 7.1, did not require solution of an energy equation, since the temperature history of the foam samples were specified. However, the regression of the decomposition front depends on the thermophysical properties of the foam, as well as the decomposition mechanism. Temperature dependent thermophysical properties for a rigid polyurethane foam are given in Table 5. The temperature dependent thermal conductivity and the heat capacity were measured[23] with a differential scanning calorimeter and a laser flash technique, respectively.

Table 5. Thermophysical properties of foam

Variable Symbol	Description	Nominal Value
ρ_o	Foam density, g/cm^3	0.353
k_f	Thermal conductivity,[5] cal/s-cm-K	
	23˚ C	1.4×10^{-4}
	50˚ C	1.5×10^{-4}
	100˚ C	1.6×10^{-4}
	150˚ C	1.8×10^{-4}
	200˚ C	2.0×10^{-4}
	250˚ C	2.2×10^{-4}
c_{pf}	Heat capacity,[5] cal/g-K	
	23˚ C	0.303
	50˚ C	0.324
	100˚ C	0.358
	150˚ C	0.440
	200˚ C	0.475
	250˚ C	0.526

Two different rates were investigated: 1) a fast burn rate (0.97±0.14 cm/min) obtained using a a radiative boundary condition with a source temperature of 1,000˚ C and 2) a slow burn rate (0.26±0.05 cm/min) obtained using a constant flux boundary condition of 0.5 cal/cm^2-s. All the simulations in this section were made using 0.5-mm elements. The gradient of the object function with respect to model parameters, $dV/d\zeta_i$, was used to determine the uncertainty in foam recession rate with the following equation:

$$(\Delta V)^2 = \sum_{i=1}^{n} \left(\zeta_i \frac{dV}{d\zeta_i} \cdot \frac{\Delta\zeta_i}{\zeta_i} \right)^2, \tag{51}$$

where V, ζ_i, ΔV, and $\Delta\zeta_i$ represent the foam recession rate, the i^{th} model parameter, uncertainty in foam recession rate, and the uncertainty in the i^{th} parameter, respectively. The subscript i represents the initial density of the foam, the conductivity of the foam, the heat capacity of the foam, the initial temperature of the foam, the activation energies of the nine PUF reactions, the decomposition enthalpy, and the emissivity of the foam. Since the thermal conductivity and heat capacity of the foam are temperature dependent, the sensitivity parameter for these variables was modified by using a multiplying factor to scale the temperature-dependent property. The scale factor for both the thermal conductivity and specific heat was chosen to be one. A similar approach was used for the reaction enthalpy.

Table 6 gives the 15 parameters used in the response derivative analysis of the fast burn rate obtained using the one-dimensional burn model with a radiative boundary condition. The nominal parameter values, ζ_i; the gradient of the foam recession rate, $dV/d\zeta_i$; the estimated parameter uncertainty, $\Delta\zeta_i$; and the individual variable uncertainty, $\left(\zeta_i \frac{dV}{d\zeta_i} \cdot \frac{\Delta\zeta_i}{\zeta_i}\right)^2$; are also given in Table 6. The contributions to the overall uncertainty is shown in parenthesis in Table 6. Variables with a contribution to the overall uncertainty greater than 5% are shaded. The most sensitive variables affecting foam recession rate for the case with the radiative boundary condition are the activation energies associated with the Reactions (2), (4), and (5) as given in Table 1. These are the same kinetic variables that were determined to be the most sensitive kinetic variables in the Plackett Burman analysis discussed in Section 7.1. A one percent change in model parameters resulted in a 14% change in the high foam recession rate case.

Table 6. Uncertainty Analysis for Radiation Boundary Condition*

i	ζ_i	$dV/d\zeta_i$	$\Delta\zeta_i$	$\zeta_i \frac{dV}{d\zeta_i} \cdot \frac{\Delta\zeta_i}{\zeta_i}$, cm^2/min^2
ρ_o	0.353 g/cm^3	9.93×10^{-1}	$0.01\times\zeta_i$	0.0000123 (0.1%)
k_f	1.0	2.93×10^{0}	$0.01\times\zeta_i$	0.0008601 (4.4%)
c_{pf}	1.0	1.90×10^{0}	$0.01\times\zeta_i$	0.0003626 (1.9%)
T_o	300 K	-8.59×10^{-3}	$0.01\times\zeta_i$	0.0006648 (3.4%)
E_1	53400 cal/mol	-1.94×10^{-5}	$0.01\times\zeta_i$	0.0001071 (0.6%)
E_2	44580 cal/mol	-9.90×10^{-5}	$0.01\times\zeta_i$	**0.0019478 (10.0%)**
E_3	42520 cal/mol	7.33×10^{-6}	$0.01\times\zeta_i$	0.0000097 (0.0%)
E_4	45900 cal/mol	-2.30×10^{-4}	$0.01\times\zeta_i$	**0.0111401 (57.3%)**
E_5	44600 cal/mol	1.28×10^{-4}	$0.01\times\zeta_i$	**0.0032844 (16.9%)**
E_6	58060 cal/mol	2.79×10^{-5}	$0.01\times\zeta_i$	0.0002632 (1.4%)
E_7	51850 cal/mol	2.32×10^{-5}	$0.01\times\zeta_i$	0.0001449 (0.7%)
E_8	52830 cal/mol	-2.31×10^{-5}	$0.01\times\zeta_i$	0.0001492 (0.8%)
E_9	56660 cal/mol	-3.10×10^{-5}	$0.01\times\zeta_i$	0.0003085 (1.6%)
h_{rf}	-35 cal/cm^3	3.49×10^{-2}	$0.01\times\zeta_i$	0.0001492 (0.8%)
ε	0.8	7.56×10^{-1}	$0.01\times\zeta_i$	0.0000366 (0.2%)
				$\Sigma =$ **0.01944 (100%)**

* The foam recession rate for a radiation boundary, with source temperature of 1,000 ˚C, is 0.97±0.14 cm/min.

The sensitivity of the PUF model parameters to a moderate boundary condition of 0.5 cal/cm^2-s was also investigated. The moderate boundary condition resulted in a thicker reaction zone making variables such as thermal conductivity more significant. As highlighted in Table 7, the most sensitive variables affecting foam recession rate for the constant flux calculation are the initial density, thermal conductivity, kinetics effecting the formation and destruction of the secondary polymer, and the reaction enthalpy. A one percent variation in the input factors resulted in a 18% change in the foam recession rate. The sensitivity of the model to input param-

Table 7. Uncertainty Analysis for Constant Flux Boundary Condition*

i	ζ_i	$dV/d\zeta_i$	$\Delta\zeta_i$	$\zeta_i \frac{dV}{d\zeta_i} \cdot \frac{\Delta\zeta_i}{\zeta_i}\Big)$, cm^2/min^2
ρ_o	0.353 g/cm^3	-4.51×10^{0}	$0.01\times\zeta_i$	**0.0002540 (11.1%)**
k_f	1.0	1.09×10^{0}	$0.01\times\zeta_i$	**0.0001178 (5.1%)**
c_{pf}	1.0	1.48×10^{-1}	$0.01\times\zeta_i$	0.0000022 (0.1%)
T_o	300 K	-3.09×10^{-3}	$0.01\times\zeta_i$	0.0000862 (3.8%)
E_1	53400 cal/mol	2.53×10^{-6}	$0.01\times\zeta_i$	0.0000018 (0.1%)
E_2	44580 cal/mol	-1.68×10^{-5}	$0.01\times\zeta_i$	0.0000561 (2.5%)
E_3	42520 cal/mol	-6.30×10^{-6}	$0.01\times\zeta_i$	0.0000072 (0.3%)
E_4	45900 cal/mol	-5.20×10^{-6}	$0.01\times\zeta_i$	0.0000057 (0.2%)
E_5	44600 cal/mol	-4.16×10^{-5}	$0.01\times\zeta_i$	**0.0003446 (15.1%)**
E_6	58060 cal/mol	-2.88×10^{-5}	$0.01\times\zeta_i$	**0.0002800 (12.2%)**
E_7	51850 cal/mol	7.95×10^{-6}	$0.01\times\zeta_i$	0.0000170 (0.7%)
E_8	52830 cal/mol	-3.61×10^{-5}	$0.01\times\zeta_i$	**0.0003627 (15.9%)**
E_9	56660 cal/mol	3.06×10^{-5}	$0.01\times\zeta_i$	**0.0003012 (13.2%)**
h_{rf}	-35 cal/cm^3	6.07×10^{-2}	$0.01\times\zeta_i$	**0.0004516 (19.7%)**
				$\Sigma =$ **0.002288 (100%)**

*The foam recession rate for a constant flux of 0.5 cal/s-cm^2 is 0.26±0.05 cm/min.

eters show that the foam decomposition process is highly nonlinear. However, since the foam recession rate gradients contain both positive and negative values, the 18% variation in foam recession rate is a conservative estimate.

8. SCALE-UP EXPERIMENT

Chu et al.[10] have performed component-scale experiments of foam decomposition with well-characterized boundary conditions using a heat lamp array to produce fire-like heat fluxes.

In Fig. 17, the two-dimensional axisymmetric geometry of the foam experiment is shown with an 8.8-cm diameter by 15-cm long right circular cylinder of foam encapsulating a 3.8-cm diameter by 6.4-cm long right circular cylinder of 304 stainless steel (SS). The face of the embedded component was 3.2-cm from the heated surface. The foam cylinder was contained in a sample cup that is shown in Fig. 18. The cup consisted of a 0.95-cm thick stainless steel bottom, which was press fit into a 7.3-cm long, thin wall (0.5-mm) stainless steel tube. Six 6-mm diameter holes were drilled through the side of the stainless steel tub, near the cup bottom, to vent decomposition gases. The number and size of the vents were chosen to keep the pressure within the cup near ambient conditions to minimize mass transfer effects. Figure 19 shows the vent holes in an X-ray image of the component-scale experiment after 15-min exposure to an incident flux of 25 W/cm^2. The burn front is also visible in Fig. 19.

The white circles in Fig. 19 show the location of the thermocouples which were welded to the side of the can and the bottom of the can. The location of the thermocouples on the can are shown in more detail in the insert of Fig. 20. Figure 20 also gives the measured temperature at various axial can locations as well as the temperature of the bottom of the can for the component-scale experiment. The boundary conditions for the COYOTE simulation of the component-scale experiment were set to the specific temperatures measured along the surface of the confining cup. The cup bottom temperature was maintained at 1,000˚ C with the thermocouple located within the bottom plate as shown in Fig. 20. Figure 21 shows the measured cup wall temperatures and bottom cup temperature at early times. In Fig. 21, temperatures measured with thermocouples ❺ and ❻ should not be hotter than the temperatures measured with thermocouple ❹.

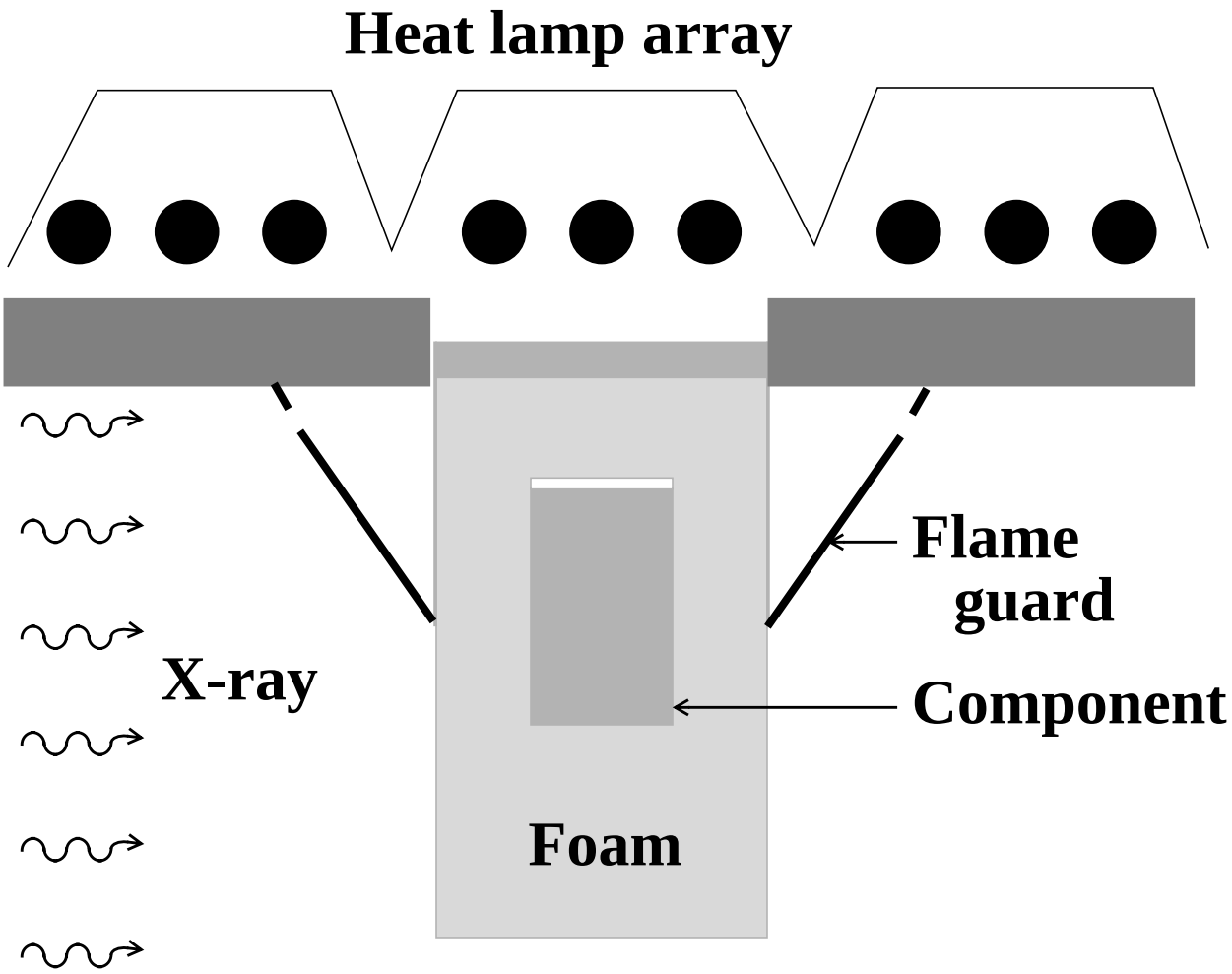

Fig. 17 Schematic of component-scale ambient-pressure vented experiment.[9]

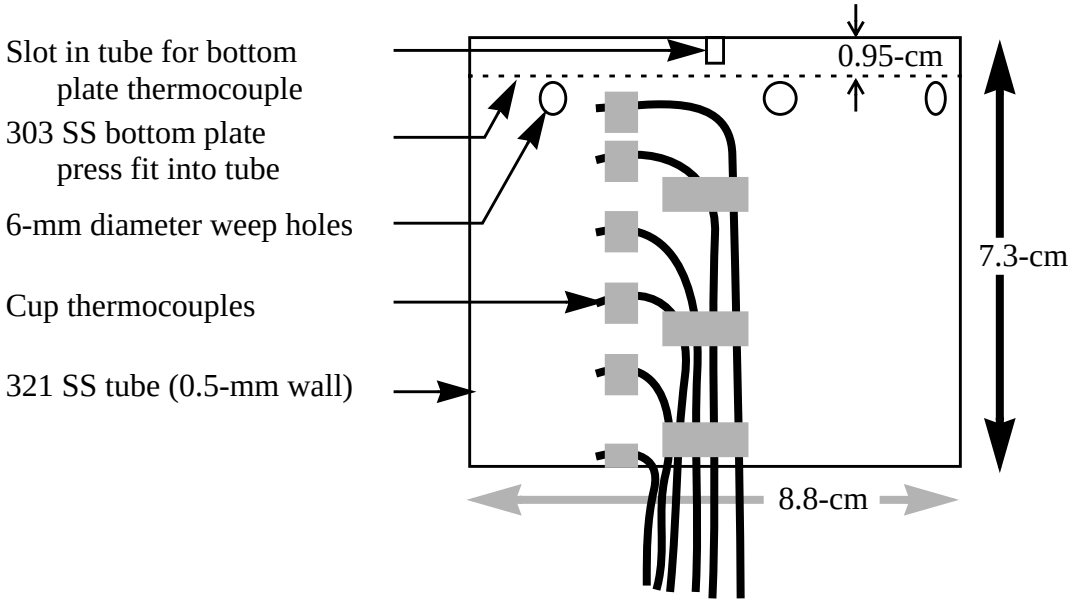

Fig. 18 Foam cylindrical holding cup. The foam (not shown) is 15-cm long and protrudes from the cup.

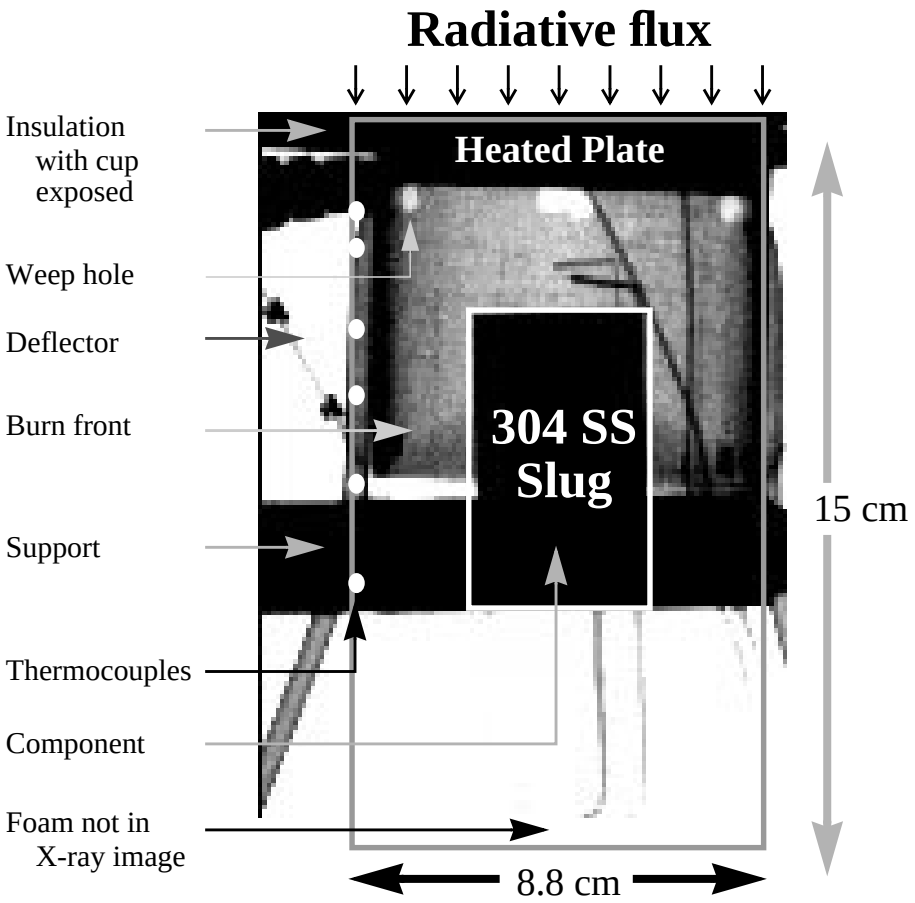

Fig. 19 X-ray image of component-scale experiment after 15-min exposure to an incident flux of 25 W/cm^2.

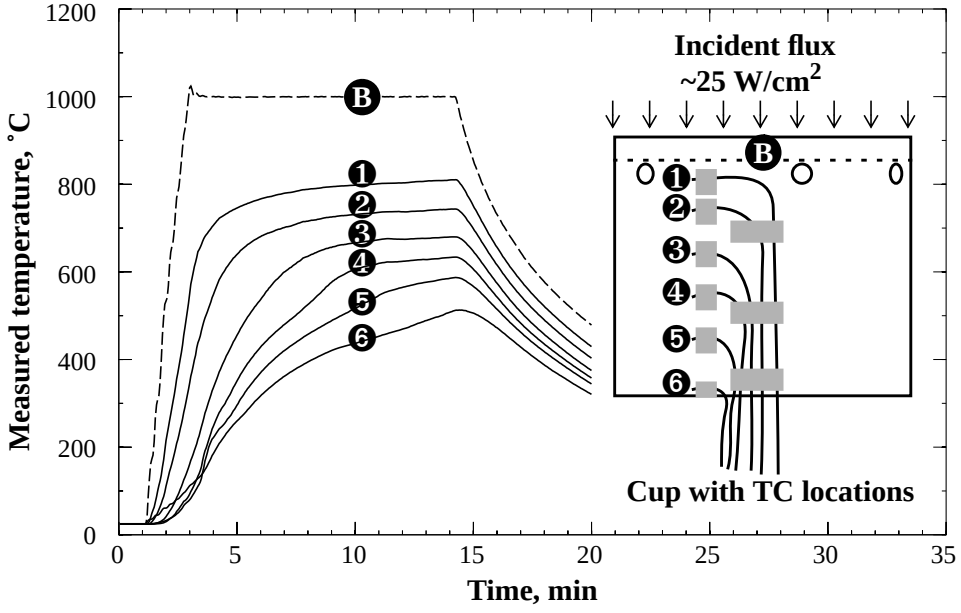

Fig. 20 Measured cup wall temperatures and bottom cup temperature.[10]

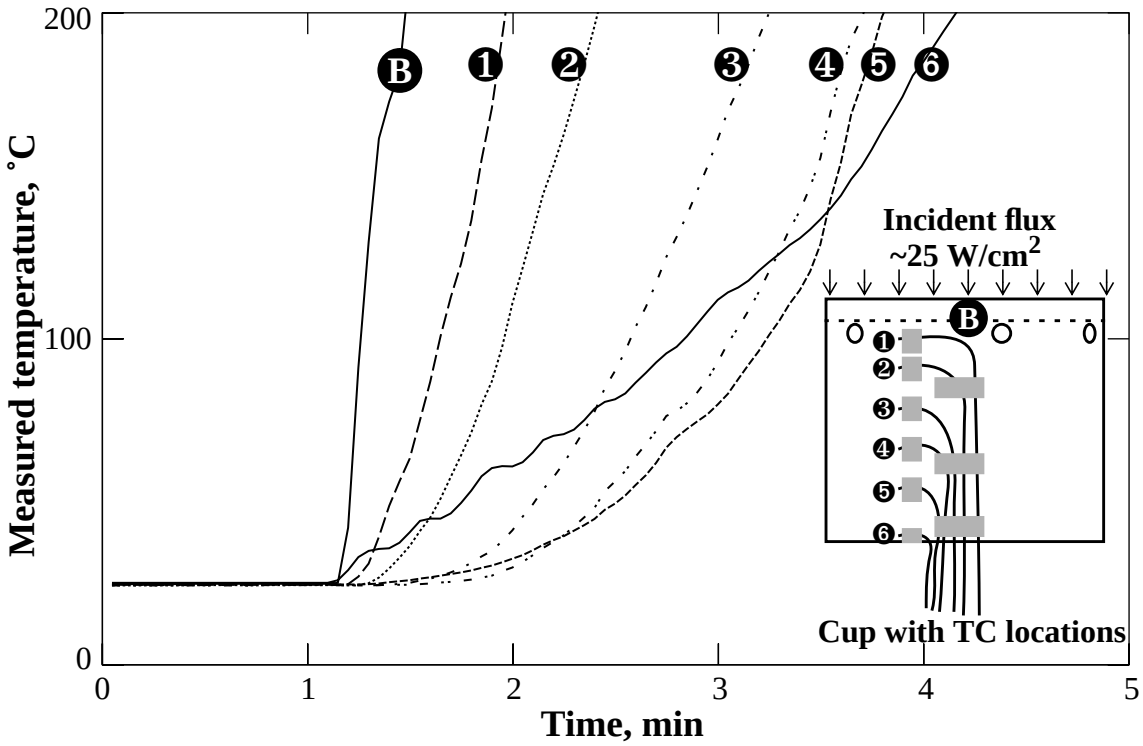

Fig. 21 Measured cup wall temperatures and top cup temperature at early times. Suspect temperatures ❺and ❻ should not be hotter than ❹.

Figure 22 shows the axisymmetric mesh and an X-ray of the foam with the encapsulated 304 SS component. A 3-mm gap was visible in the X-ray taken prior to the experiment. The 3-mm gap was modeled as a radiation enclosure. The element dimensions were chosen to be 5 mm by 5 mm to maintain at least three to four elements across the reaction zone as shown in Fig. 23. The mesh in Fig. 22 is expected to give a grid error, as defined by Eq. (50), less than 5%. The temperature and density profiles across the decomposition front are shown in Fig. 23.C. The thickness of the front estimated from Fig. 23.C is 4 mm, which confirms that the 0.5-mm element dimension is sufficiently small. Figure 23.D also shows the predicted temperature profile and solid fraction profile across the burn front. The density profile shown in Fig. 23.C has significant scatter. The density profile was estimated from the pixel density in the X-ray image shown in

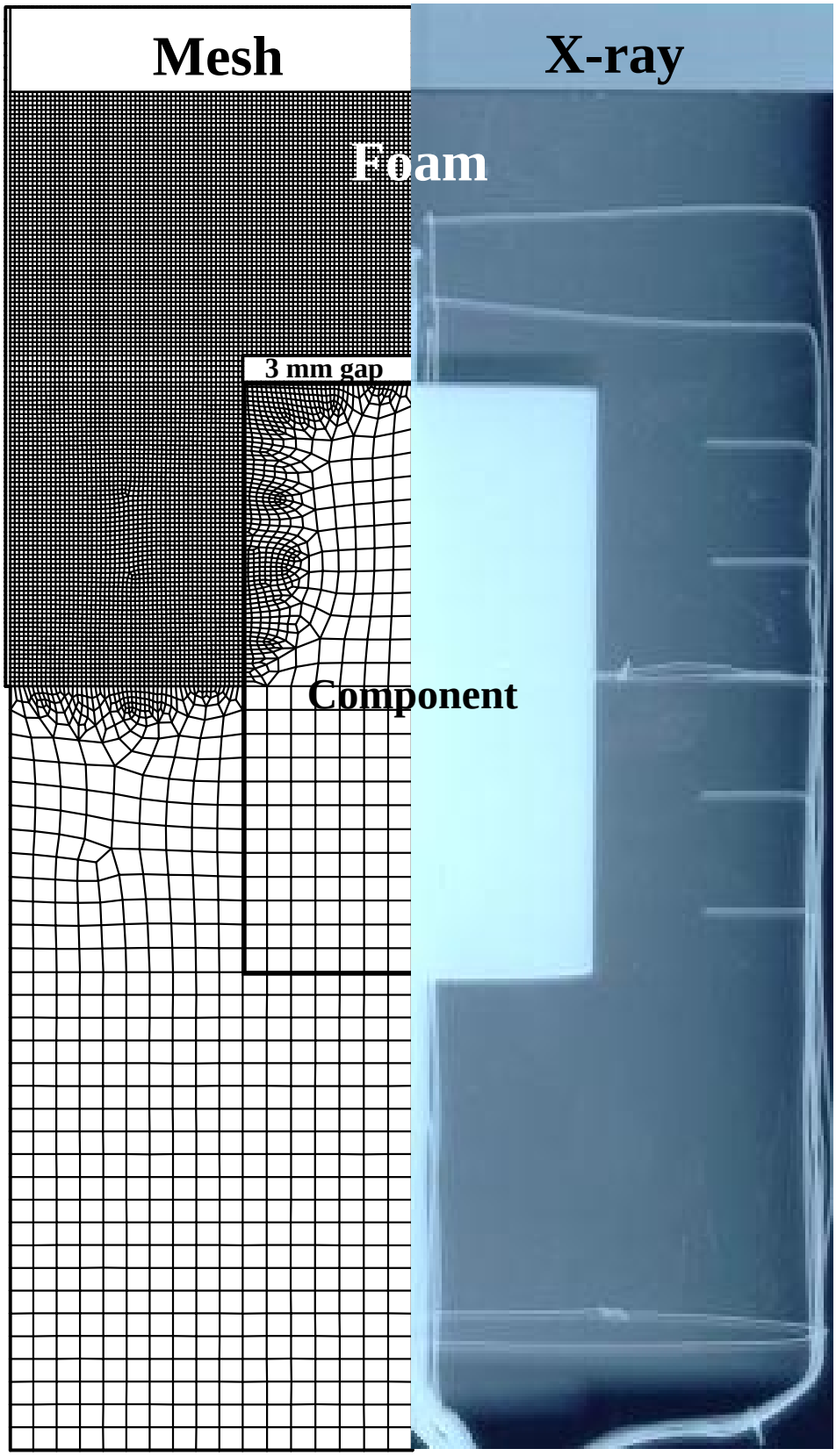

Fig. 22 Axisymmetric mesh with 11,209 elements and X-ray of foam in cylindrical holding cup showing 3 mm gap between face of component and foam. The foam is 15-cm (6 inches) long and protrudes from the cup.

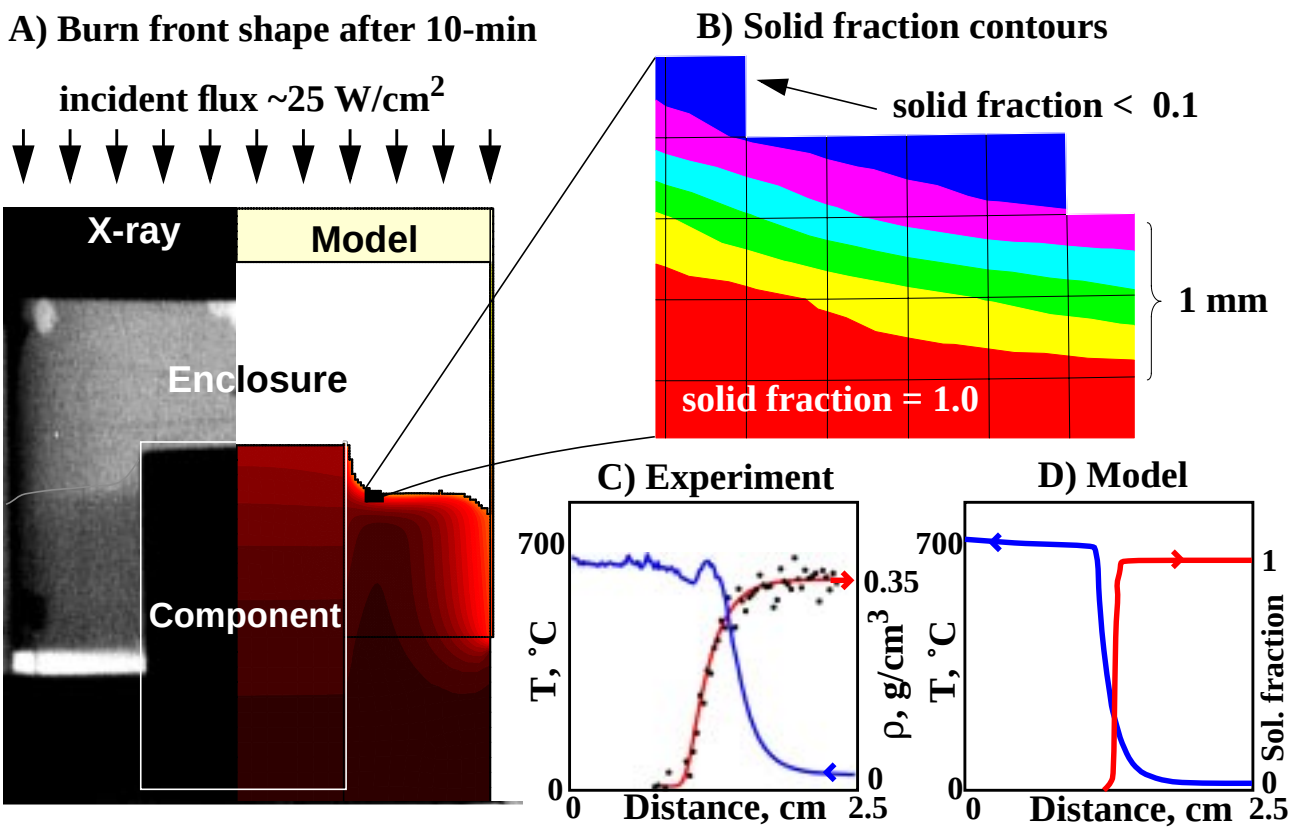

Fig. 23 A) Measured and predicted burn front shape after 10-min exposure to an incident flux ~25 W/cm^2, B) predicted solid fraction contours, C) measured temperature and density across burn front, and D) predicted temperature and solid fraction across burn front.

Fig. 23.A. Despite this uncertainty, the measured density profile and the predicted solid fraction profile across the burn front are similar.

Figure 24 shows a comparison between X-ray images and calculated temperature profiles of the foam with the cup bottom exposed to an incident flux of ~25 W/cm^2. The boundary conditions were set to the specific temperatures measured along the cup surface and bottom as shown in Fig. 20. The nominal values of the PUF model parameters given in Table 2 and the temperature-dependent thermophysical properties given in Table 5 were used for the calculations shown in Fig. 24. Resistance across the foam residue on the face of the component was also accounted for by assuming a reduced component surface emissivity of 0.6. The reaction enthalpy was cho-

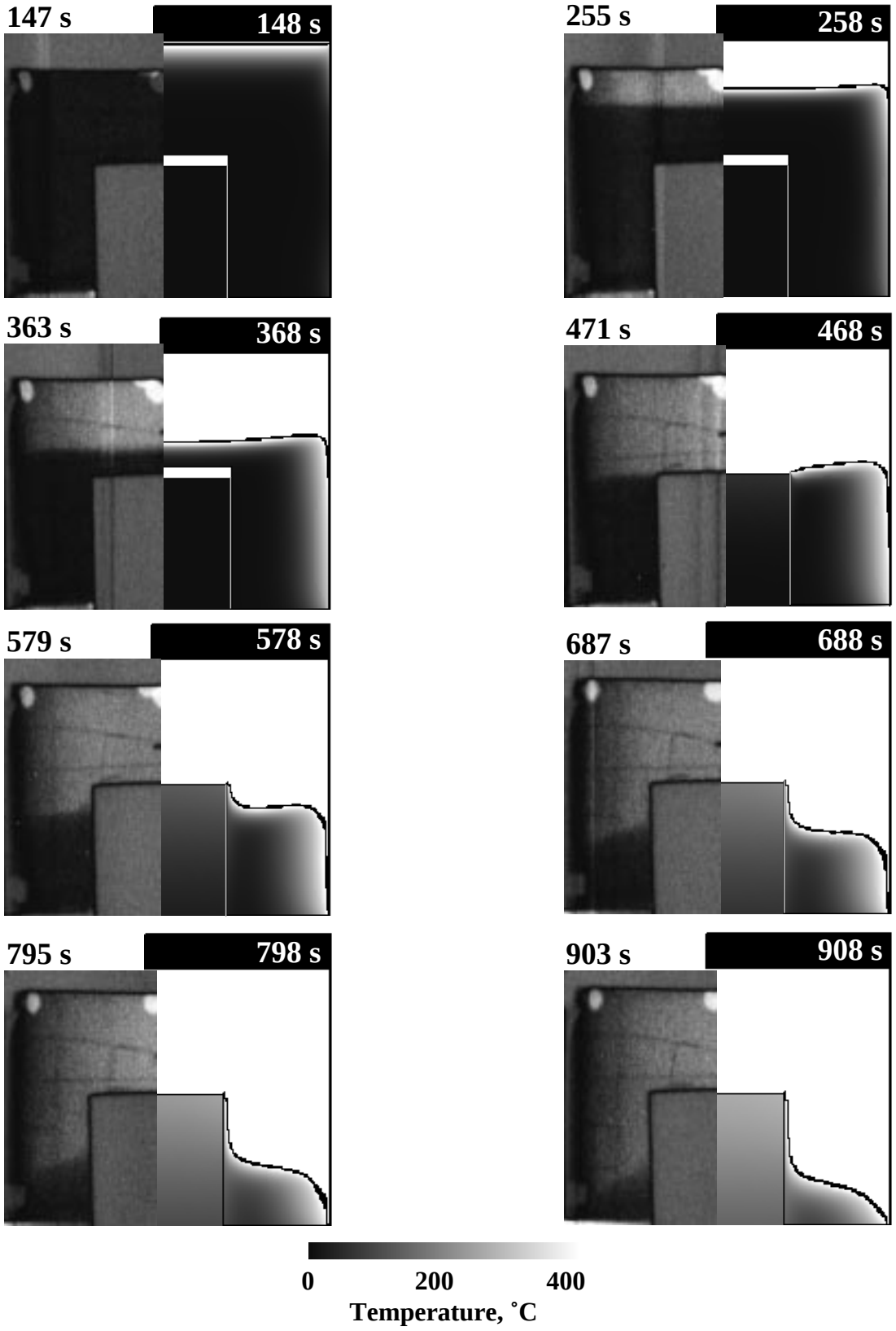

Fig. 24 X-ray images (left) and calculated temperature profiles (right) of foam with cup bottom exposed to an incident flux of ~25 W/cm^2.

sen to be consistent with bond energies of polyatomic compounds. In Fig. 24, the decomposition front is horizontal prior to reaching the component. As the front gets closer to the embedded component, the decomposition front curves around the component. The exact location of the decomposition front is seen as a density variation in the X-rays. COYOTE's element death option was used to remove elements when the condensed fraction within individual elements was less than 0.01. The shape of the front is difficult to determine near the wall in the X-rays because of the curvature of the confinement. Nevertheless, the calculated and measured shape of the decomposition front appear to *agree very well*.

Figure 25 shows the location of the thermocouples at the center and midradial positions. Figures 26, 27, and 28 show a comparison between predicted and measured center, midradial, and component temperatures, respectively. The encapsulated component appears to heat up the bulk of the foam as shown by the temperature profile labeled ❿ in Fig. 26. In previous experiments without an encapsulated component,[10] all temperature measurements remained essentially constant until the decomposition front was within close proximity. With the encapsulated component, the temperature at the various thermocouple locations is shown to increase gradually until the decomposition front is within close proximity, and the temperature increase is more rapid. This behavior is shown to be more pronounced in the experimental temperature profiles plotted in Figs. 26 and 27. In Fig. 26, the temperature measured by thermocouple ❿ appears to be 100 ˚C higher than the predicted temperature at that location. This difference between the measurement and calculation is thought to be related to premature exposure of the thermocouple sheath, as shown in Fig. 29, to the hot radiating can and subsequent heat transfer by conduction to the thermocouple tip. Since the foam burns faster along the wall than in the center of the foam, the thermocouples are likely to become partially exposed. The exposed thermocouples can become hot

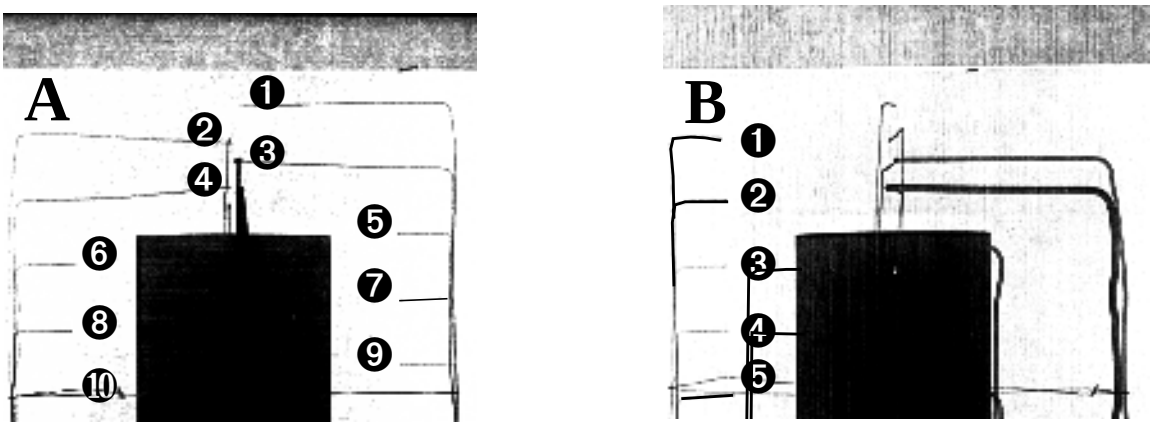

Fig. 25 A) Center thermocouple locations and B) midradial thermocouple locations.

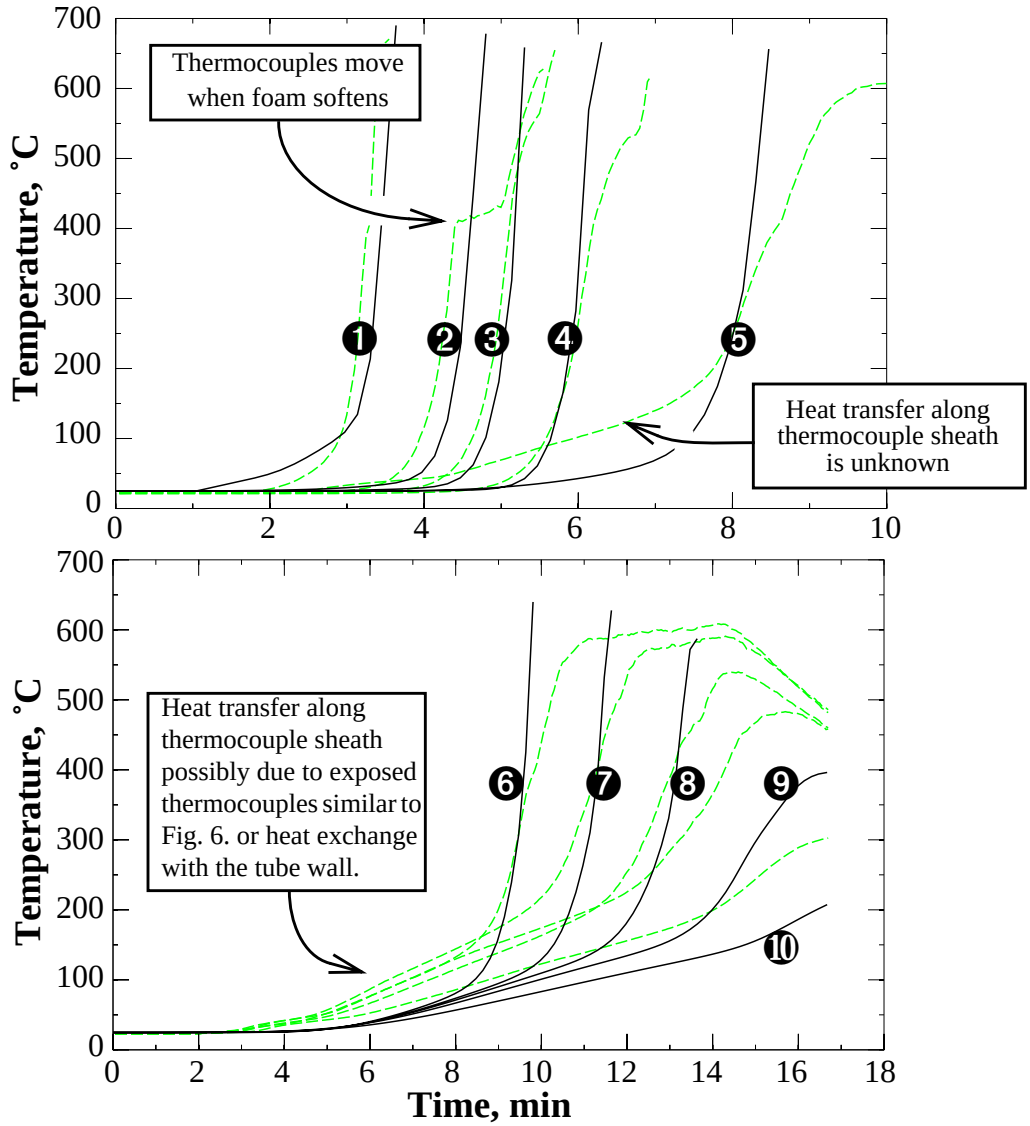

Fig. 26 Calculated (solid lines) and measured (dashed lines) temperatures at center thermocouple locations shown in Fig. 25.A.

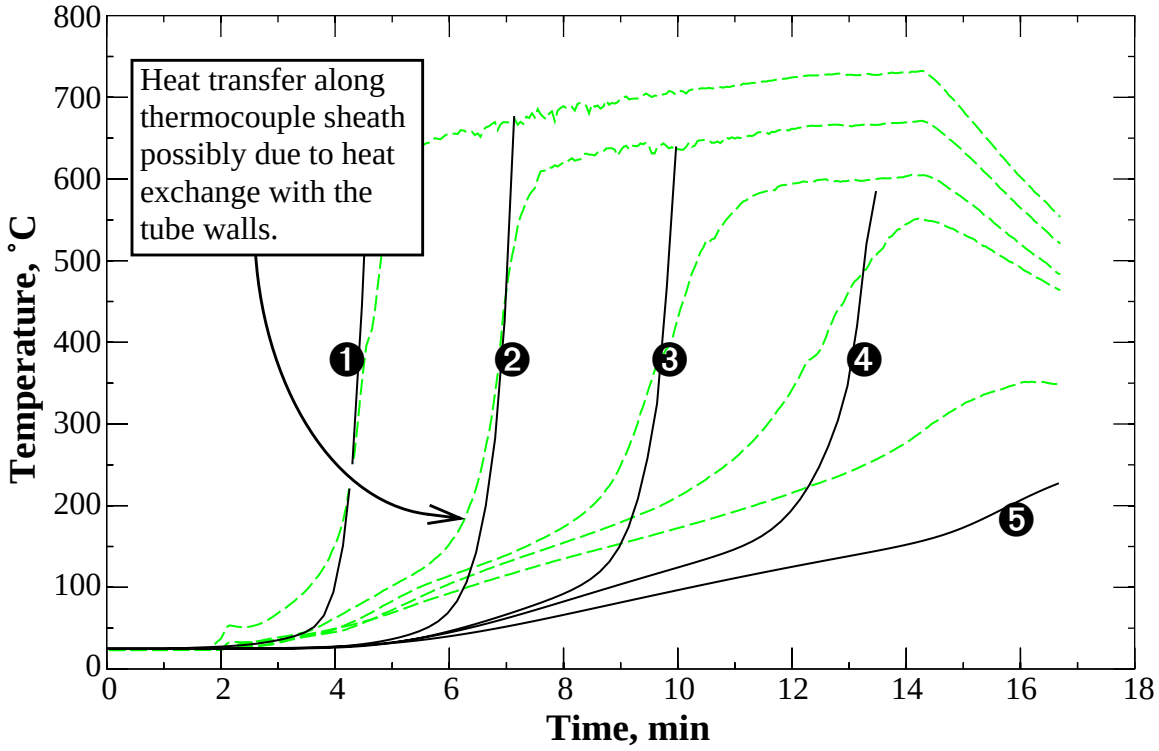

Fig. 27 Calculated (solid lines) and measured (dashed lines) temperatures at midradial thermocouple locations shown in Fig. 25.B.

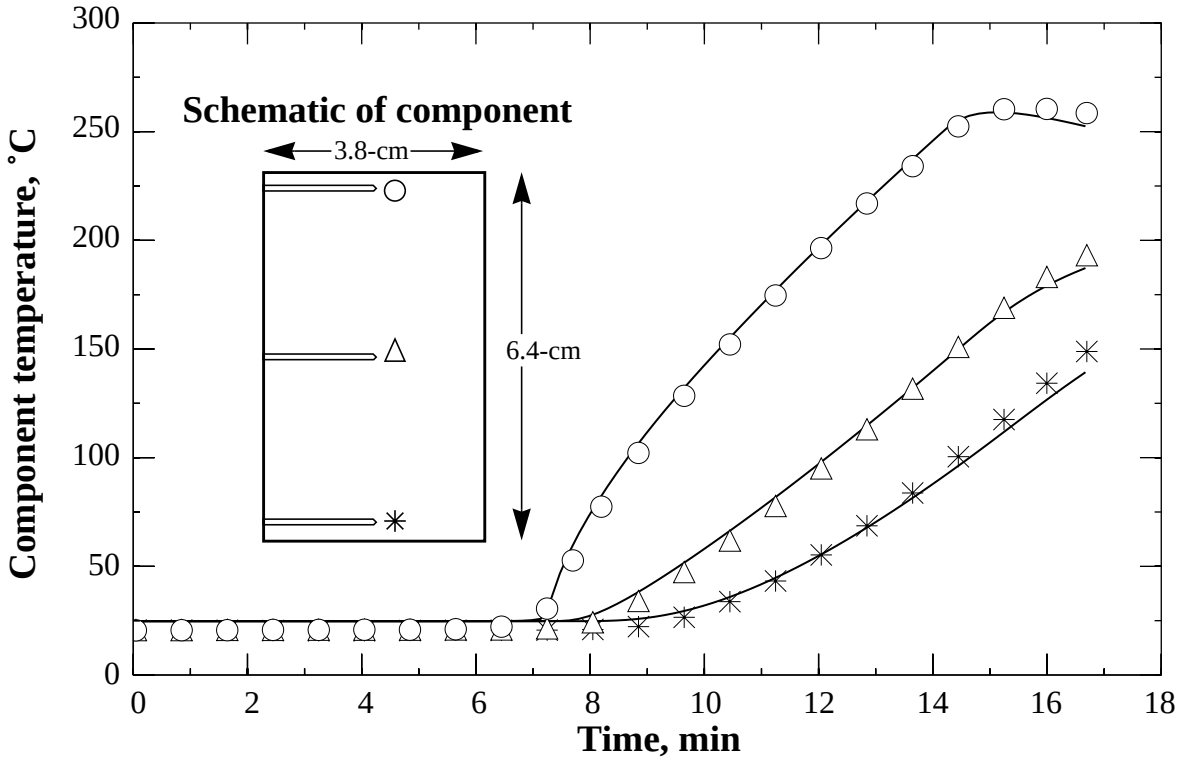

Fig. 28 Calculated (lines) and measured (symbols) temperatures of the encapsulated component at the locations indicated in the inset.

A) Top view of exposed thermocouple

B) Side view of exposed thermocouple

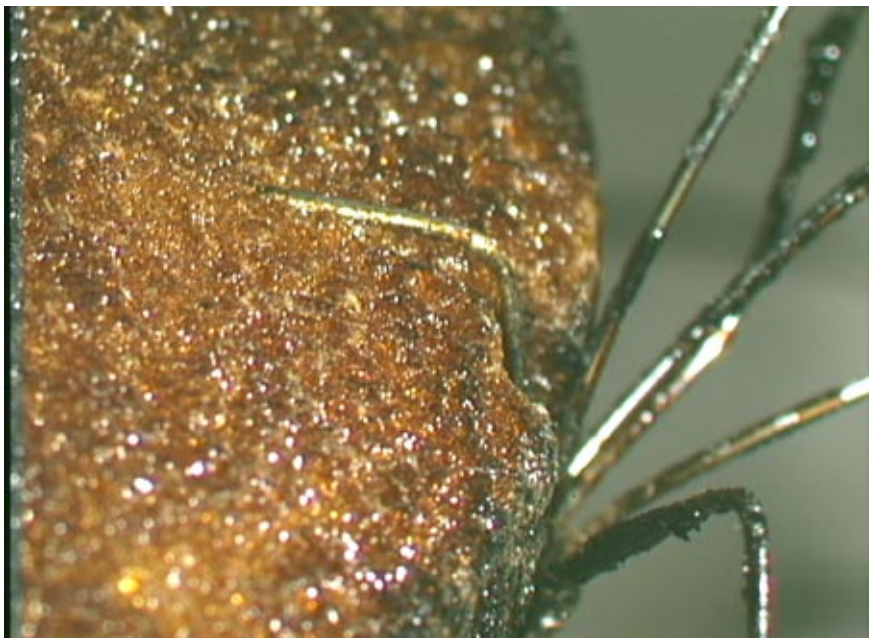

Fig. 29 A) Top view of exposed thermocouple and B) side view of exposed thermocouple.

by radiative energy exchange with the hot boundary. Furthermore, heat transfer between the hot tube walls and the thermocouple leads may have also resulted in unaccounted heat transfer to the thermocouple junctions.

Figure 30 shows the predicted transmitted heat flux along the center of the foam at various times. The maximum transmitted heat flux within the foam at each time plotted in Fig. 30 was located at the burn front. Furthermore, the overall maximum transmitted heat flux through the foam for all times occurred at early times when the foam surface was intimate with the heated surface. As the burn front moved away from the heated surface, the maximum transmitted heat flux decreased. The decrease in maximum transmitted heat flux is likely due to view factor effect since gas opacity and convective heat transfer was not included in the model.

Figure 31 shows the predicted center and midradial burn front velocities. The velocities were estimated using the time of element death. The center burn front velocity was slightly greater than the midradial burn velocities, resulting in a curved burn front shown previously in Fig. 24. The center burn front velocity profile stops at about 7 minutes when the burn front reaches the embedded component.

The 2-D axisymmetric mesh contained 11,209 elements as shown in Fig. 22. The simulation required 11 days and 16 hours of CPU time on a single processor, 3 days 16 hours of CPU time on four processors, and 2 days 1 hour on eight processors. Ninety percent of the CPU time was attributed to the view factor computation, while only nine percent of the computation was attributed to the PUF decomposition model. Adaptive gridding would reduce the chemistry computation considerably and increase simulation accuracy, but the view factor CPU time would likely increase. The view factor calculation would dramatically increase if the adaptive grid refinement approaches resolution scales defined in Section 7.2.

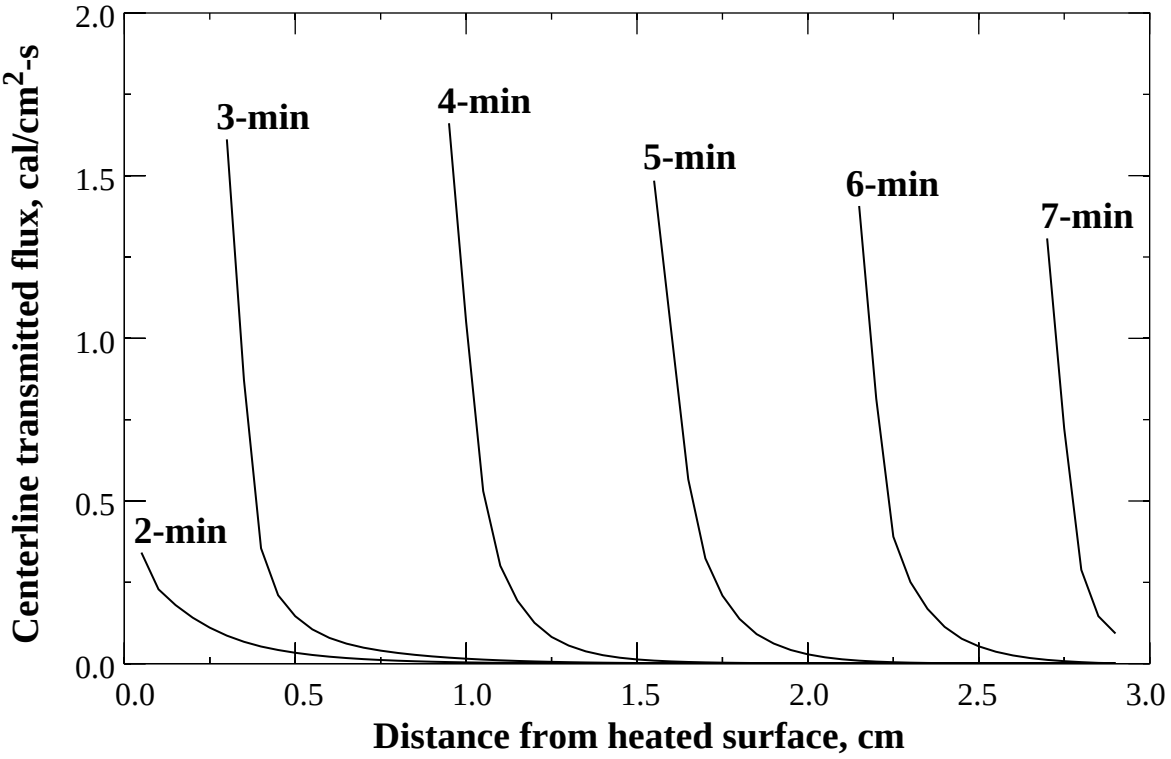

Fig. 30 Predicted transmitted heat flux along the center of the foam.

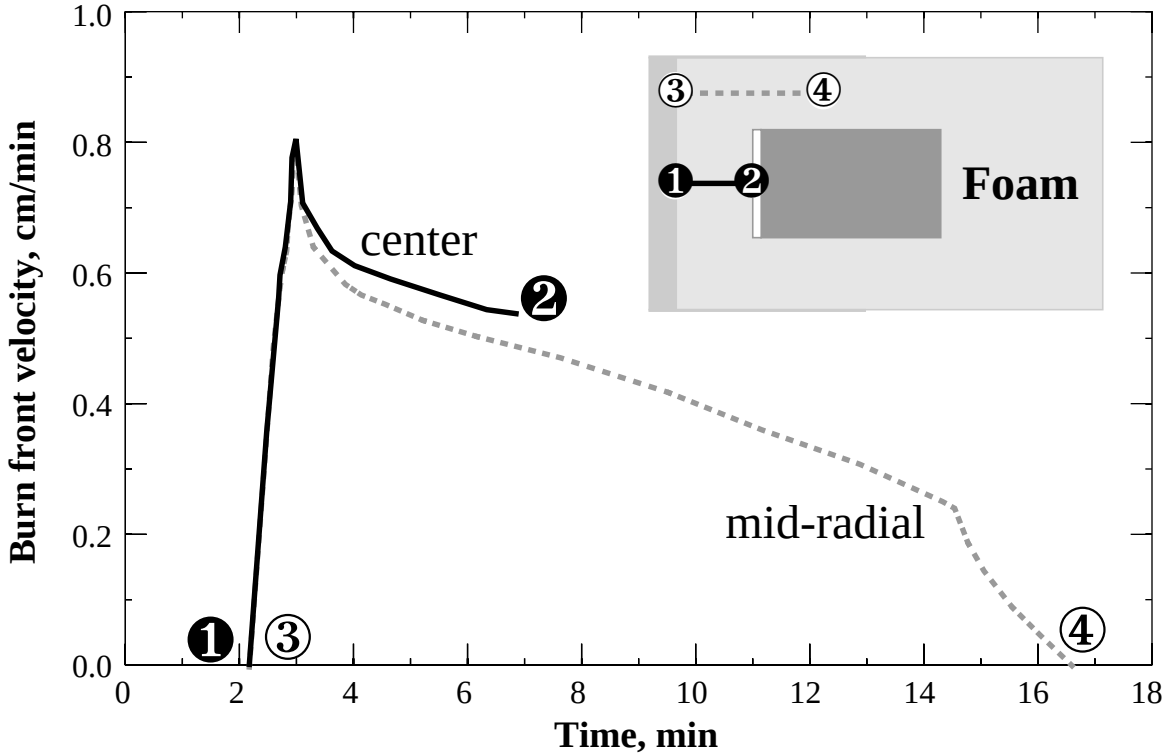

Fig. 31 Predicted center and mid-radial burn front velocity. The center and mid-radial locations are shown in the inset.

9. SUMMARY AND CONCLUSIONS

The PolyUrethane Foam (PUF) decomposition model has been applied to thermal decomposition of rigid polyurethane foam using the three-dimensional finite element code COYOTE. The PUF model is comprised of a kinetic mechanism that describes bond breaking, a lattice statistics model to describe the mass fraction of finite polymer fragments isolated from the macromolecule by broken bonds, and a transport model to describe the evaporation of the finite polymer fragments with high vapor pressures into the gas phase. The chemical structure of the rigid polyurethane foam was determined from specific synthesis procedures, and the PUF model parameters were obtained from the most probable structural units of the foam. Kinetic parameters, for the PUF bond-breaking mechanism, were obtained by using an object-oriented optimization code, used to minimize the difference between weight loss measured in a small-scale Thermal Gravimetric Analysis (TGA) apparatus using nominally 5-mg samples from six isothermal experiments[10] and model predictions. The temperature-dependent thermal conductivity and heat capacity were measured[23] with a differential scanning calorimeter and a laser flash technique, respectively. The reaction enthalpy was obtained from a differential scanning calorimeter.[10] Three nonisothermal experiments, not used to estimate kinetic parameters, were simulated to validate the selection of the kinetic parameters for the PUF model.

Various sensitivity and uncertainty analysis were performed using the PolyUrethane Foam (PUF) decomposition model. Although exact agreement between experimental data and predictions were not obtained in this study, uncertainty in both experiment and model have been explored and quantified. In the experiments, a few of the thermocouples used to define the

boundary conditions were shown to unexpectedly increase in temperature. Nonuniform burn fronts exposed thermocouple sheaths to the hot boundary. Conduction of heat along the thermocouple sheath to the thermocouple tip may have caused the measured thermocouple to read higher temperatures than the surrounding foam. Heat transfer between the hot tube walls and the thermocouple leads may have also resulted in unaccounted heat transfer to the thermocouple junctions. The uncertainty in the exposed thermocouples are on the order of 100 ˚C. Future experiments will use more thermocouples to better defined boundary conditions.

Two separate methods were used to determine model sensitivity with similar results: 1) a variance analysis and 2) a response derivative analysis. The variance analysis, based on experimental design techniques, was used to determine variables that have primary effects on the condensed fraction predicted using a 20 ˚C/min temperature ramp. The primary effect variables included the initial polymer structure and the kinetics associated with the formation of a secondary polymer. Two response derivative analysis were performed by calculating the gradient of the foam recession rate with respect to model parameters for a fast regression (0.97±0.14 cm/min) obtained using fire-like boundary conditions and a slow regression (0.26±0.05 cm/min) obtained using a mild, constant flux boundary condition. For the fast regression, the most sensitive kinetic parameters were associated with the formation of the secondary polymer in agreement with the Plackett Burman analysis. For the slow regression, the reaction zone thickened; and thermal conductivity, initial density, and reaction enthalpies were shown to be sensitive parameters as well as the activation energies associated with the destruction of the secondary polymer. The response derivatives were significantly different for the fast regression case than the slow regression case. Different conditions will undoubtedly give different sensitivity results.

A two-dimensional axisymmetric simulation of an unconfined, component-scale experiment was performed using an 11,209 element mesh with the PUF model implemented into COY-

OTE.[1] The simulation of decomposing polyurethane foam around an encapsulated component included a 3-mm gap at the face of the cylindrical component. Predictions were made using a grid-independent solution with 0.5-mm by 0.5-mm elements and compared to experimental temperature measurements. Elements were removed from the computational domain whenever the condensed fraction was less than 0.01, and view factors were recomputed. Good agreement was obtained between temperature measurements and predictions. The shape of the regression front measured with X-ray imaging was also in agreement with the predicted shape of the regression front. Although the agreement between the predicted and measured temperatures was not exact, the temperatures are within experimental and computational uncertainty.

10. ACKNOWLEDGEMENTS

The authors gratefully acknowledge the technical assistance provided by J. H. Bentz, W. Gill, L. L. Humphries, and J. G. Pantuso (scale-up experiments), T. A. Ulibarri and T. Neet (provided foam samples and synthesis details), R. S. Saunders (polymer structures and synthesis of model compounds for IR analysis), T. T. Borek (desorption tube analysis), J. N. Castaneda (TGA analysis), and J. D. Kurtz (currently with Proctor and Gamble). Modeling discussions related to percolation theory with D. M. Grant (University of Utah), R. J. Pugmire (University of Utah), and T. H. Fletcher (Brigham Young University) are also appreciated. Discussions regarding uncertainty and sensitivity analysis with M. R. Baer and B. F. Blackwell were helpful. M. S. Eldred helped set up the DAKOTA optimizer used to obtain the activation energies and the object function gradients used in the uncertainty analysis. Comments from internal reviewers at Sandia National Laboratories, A. R. Kerstein, L. M. G. Minier, Jaime Moya, and A. C. Ratzel, are also deeply

appreciated. D. K. Gartling performed the three-dimensional calculations shown in Fig. 1, and R. J. Pugmire provided the solid state NMR analysis shown in Fig. 6.C.

11. REFERENCES

1. Gartling, D. K., Hogan, R. E. & Glass, M. W., "COYOTE - A Finite Element Computer Program for Nonlinear Heat Conduction Problems," SAND94-1173 (theory), SAND94-1179 (user's manual), Sandia National Laboratories, Albuquerque, NM (1998).

2. Solomon, P. R., Hamblen, D. G., Carangelo, R. M., Serio, M. A. & Deshpande, G. V., *Energy & Fuels*, **2** (1988) 405.

3. Grant, D. M., Pugmire, R. J., Fletcher, T. H. & Kerstein, A. R., *Energy & Fuels*, **3** (1989) 175.

4. Fletcher, T. H., Kerstein, A. R., Pugmire, R. J. & Grant, D. M., *Energy & Fuels*, **4** (1990) 54.

5. Fletcher, T. H., Kerstein, A. R., Pugmire, R. J., Solum, M. S. & Grant, D. M., *Energy & Fuels*, **6** (1992) 414.

6. Fisher, M. E. & Essam, J. W., *Journal of Mathematical Physics*, **2** (1961) 609.

7. Flory, P. J., *Principles of Polymer Chemistry*, Cornell University Press, Ithaca, New York (1953) 347.

8. Solum, M. S., Pugmire, R. J. & Grant, D. M., *Energy & Fuels*, **3** (1989)187.

9. Shafizadeh, F., "The Chemistry of Pyrolysis and Combustion," Ch. 13 in *The Chemistry of Solid Wood*, Advances in Chemistry Series 207, Rowell, R., editor, American Chemical Society, Washington, D. C. (1984).

10. Chu, T. Y., Hobbs, M. L., Erickson, K. L., Ulibarri, T. A., Renlund, A. M., Gill, W., Humphries, L. L. & Borek, T. T., *SAMPE 1999 - 44th International SAMPE Symposium & Exhibition*, Long Beach, CA (1999).

11. Shampine, L. F. & Watts, H. A., "DEPAC - Design of a User Oriented Package of ODE Solvers," SAND-79-2374, Sandia National Laboratories, Albuquerque, NM (1979).

12. Solomon, P. R., Hamblen, D. G., Serio, M., Yu, Z. & Charpenay, S., *Fuel*, **72** (1993) 469.

13. Kerstein, A. R., *J. Phys. A: Math. Gen.*, **22** (1989) 3371.

14. Solomon, P. R., Hamblen, D. G., Yu, Z. Z. & Serio, M. A., *Fuel*, **69** (1990) 754.

15. Suuberg, E. M., *Chemistry of Coal Conversion*, R. H. Schlosberg (Ed.) Plenum Press, New York (1985).

16. Atkins, P. W., *Physical Chemistry*, second edition, W. H. Freeman and Company, San Francisco, California (1982).

17. Henley, E. J., & Seader, J. D., *Equilibrium-Stage Separation Operations in Chemical Engineering*, John Wiley & Sons, New York (1981).

18. Shampine, L. F., & Watts, H. A., "ZEROIN - A Root-Solving Code," SC-TM-70-631, Sandia National Laboratories, Albuquerque, NM (1970).

19. Daubert, T. E., Danner, R. P., Subul, H. M., and Stebbins, C. C., *Physical and Thermodynamic Properties of Pure Compounds: Data Compilation*, Taylor & Francis, Bristol, PA (1994). See also Daubert, T. E. and Danner, R. P., *Design institute for physical property data*, AIChE, Dept. of Chem. Eng., Penn State University (1994).

20. Eldred, M. S., "Optimization Strategies for Complex Engineering Applications," SAND98-0340, UC-705, Sandia National Laboratories, Albuquerque, NM (1998).

21. Erickson, K. L. et al., "Tentative title: Decomposition of a Rigid Polyurethane Foam," to be submitted to *Polymer Degradation and Stability* (1999).

22. Wheeler, D. J., *Understanding Industrial Experimentation*, Second Edition, SPC Press, Inc., Knoxville, TN (1990). See also Notes from "Strategy of Experimentation," copyright held by E. I. duPont de Nemours and Co., Wilmington, Delaware, 19898, in October 1975 (revised edition).

23. Tayler, R. E., Groot, and Ferrier, J., "Thermophysical Properties of a Foam," TPRL 1833, Thermophysical Properties Research Laboratory, Purdue University Research Park, West Lafayette, IN (1997).

Distribution

Brigham Young University (3)
Attn: Thomas H. Fletcher
Dan Clayton
L. Douglas Smoot
Department of Chemical Engineering
350 Clyde Building
Provo, UT 84602

Federal Aviation Administration (1)
Attn: Richard E. Lyon
Fire Safety Section, AAR-422
William J. Hughes Technical Center
Atlantic City International Airport, NJ 08405

Los Alamos National Laboratory (1)
Attn: Maria Rightley
(Group XNH, MS F664)
P. O. Box 1663
Los Alamos, NM 87545

NIST (4)
United States Department of Commerce
Attn: Kathryn M. Butler
Takashi Kashiwagi
Marc Nyden
Ken Steckler
Building and Fire Research Laboratory
National Institute of Standards and Technology
Gaithersburg, MD 20899

University of California, Berkeley (1)
Attn: Carlos Fernandez-Pello
Mechanical Engineering Department
6105a Etcheverry Hall
University of California
Berkeley, CA 94720

University of Utah (1)
Attn: Ronald Pugmire
Associate Vice President for Research
Professor of Chemical & Fuels Engineering
210 Park Building
Salt Lake City, UT 84112

University of Utah (1)
Attn: David M. Grant
Distinguished Professor of Chemistry
Henry Eyring Bldg
315 S 1400 East Rm 2020
Salt Lake City, UT 84112

Internal Distribution (58)

MS	Org.	Name
1454	2554	Bonzon, L. L.
1454	2554	Renlund, A. M.
1202	5932	Ulibarri, T. A.
0343	1822	Borek, T.
0767	6314	Larsen, M. E.
1139	6423	Humphries, L. L.
9051	8351	Kerstein, A.
9052	8361	Baxter, L. L.
9052	8361	Behrens, R.
9052	8361	Margolis, S. B.
9042	8727	Ortega, A. R.
0841	9100	Hommert, P. J.
0828	9100	Bickel, T. C.
0834	9100	Baer, M. R.
0826	9100	Gartling, D. K.
0834	9100	Chu, T. Y.
0835	9111	Kempka, S. N.
0825	9111	Glass, M. W.
0834	9112	Ratzel, A. C.
0834	9112	Erickson, K. L.
0826	9113	Hermina, W.
0836	9114	Kraynik, A. M.
0825	9115	Rutledge, W. H.
0836	9116	Peterson, C. W.
0836	9116	Gill, W.
0836	9116	Gritzo, L. A.
0836	9116	Hickox, C. E.
0836	9116	Hobbs, M. L. (10)
0836	9116	Minier, L. M. G.
0836	9116	Nicolette, V. F.
0836	9116	Schmitt, R. G.
0836	9116	Tieszen, S.
0827	9117	Griffith, R.
0827	9117	Bainbridge, B. L.
0827	9117	Dempsey, F.
0827	9117	Dobranich, D.
0827	9117	Dykhuizen, R. C.
0827	9117	Gross, R. J.
0827	9117	Hogan, R. E.
0823	9123	Neilsen, M. K.
0828	9132	Moya, J. L.
0828	9133	Blackwell, B. F.
0828	9133	Dowding, K.J.
0847	9211	Eldred, M. S.
0405	12333	Jones, T. R.
9018	8940-2	Central Tech Files (1)
0899	4916	Technical Library (2)
0612	4912	Review & Approval Desk (1) for DOE/OSTI